# Supporting Information

## Anti-Kasha fluorescence, persistent room-temperature phosphorescence and delayed emission from a nearly flat non-symmetric polycyclic hydrocarbon

Monike da Silva Kutz[a,b†], Carolina Francener[c†], Wataru Ota[d,e], Manuela Santos Corrêa[a], Daniel Crane[c], Emiko Fujiwara[d], Tohru Sato[d,e$], Ivan H. Bechtold[f], Andrew P. Monkman[c#], Eduard Westphal[a*], Harald Bock[b]

[a] *Department of Chemistry, Universidade Federal de Santa Catarina, Florianópolis, Brazil*

[b] *Centre de Recherche Paul Pascal, Université de Bordeaux/Centre National de la Recherche Scientifique, Pessac, France*

[c] *Department of Physics, Durham University, Durham, United Kingdom*

[d] *Fukui Institute for Fundamental Chemistry, Kyoto University, Takano Nishibirakicho 34-4, Sakyo-ku, Kyoto 606-8103, Japan*

[e] *Department of Molecular Engineering, Graduate School of Engineering, Kyoto University, Nishikyo-ku, Kyoto 615-8510, Japan*

[f] *Department of Physics, Universidade Federal de Santa Catarina, Florianópolis, Brazil*

*$ Corresponding author: tsato@scl.kyoto-u.ac.jp*
*# Corresponding author: a.p.monkman@durham.ac.uk*
** Corresponding author: eduard.w@ufsc.br*
[†] These authors contributed equally to this work

### Content

## 1. Synthesis and Structural Characterization

Commercial reagents and solvents were used as supplied (Merck, Sigma-Aldrich, Fluka and Acros Organics). Dichloromethane (DCM) was dried using an Innovative Technology PS-MD-5 Solvent Purification System (SPS). Reactions were monitored by thin-layer chromatography (TLC) on aluminum plates coated with silica gel and UV254 nm indicator. Purifications were performed by column chromatography on silica gel (60–200mesh, 60Å); by Gel Permeation Chromatography (GPC), using a JAI FC-3480 Recycling Preparative HPLC a JAIGEL-2.5HR-40 column, with HPLC-isocratic grade chloroform stabilized with ethanol as eluent; and recrystallizations using commercial-grade solvents. Melting points were measured in a polarized optical microscope Olympus BX53 coupled to a Mettler Toledo FP-82 hot stage. $^{1}H$ and $^{13}C$ NMR spectra were recorded with a JEOL ECS-400 spectrometer operating at 400 MHz and 100.6 MHz. Infrared (IR) spectra were obtained in a Bruker spectrometer, model Alpha, using KBr pellets. Elemental analysis was performed using a Perkin-Elmer series II CHNS/O Analyzer (model 2400) coupled to a Perkin-Elmer Autobalance AD 6000. Mass spectrometry analyses were performed using a Bruker Autoflex Speed matrix-assisted laser desorption/ionization time-of-flight (MALDI-TOF) mass spectrometer (Bruker Daltonics), equipped with a 2 kHz Smartbeam-II laser system. The instrument was operated in the reflectron mode, detecting positive ions.

### *1.1. Synthesis of 2-(1-indanylidene)-1-indanone (**2**)*

Under argon atmosphere and strong stirring, a solution of 1-indanone (**1**, 3.3 g, 25 mmol) in anhydrous dichloromethane (DCM) (25 mL) was rapidly added at 0 °C via an addition funnel to a solution of $TiCl_4$ (0.13 mL, 1.2 mmol) in hexane (5 mL) . Subsequently, a second equivalent of 1-indanone (**1**, 3.3 g, 25 mmol), along with triethylamine (3.8 mL, 27.5 mmol) in anhydrous DCM (25 mL), was added dropwise over a period of 20 minutes. After complete addition, the dark-green mixture was stirred at 0 °C for 30 minutes and then at 298 K for 16 hours[1]. Afterward, the mixture was slowly poured into acetone (75 mL), the precipitate was filtered and washed with hot ethanol (100 mL). The light-yellow remaining solid was purified by recrystallization from toluene (150 mL).

**Yield**: 2.46 g (246.3 g $mol^{-1}$, 10 mmol, 40%) of a light-yellow solid. $\mathbf{R_f}$ = 0.5 (50% DCM:petroleum ether (PE)); **m.p**.: 144 – 146 ºC (lit. 143 – 144 °C)[2,3]; **$^{1}$H NMR** ($CDCl_3$, 400 MHz, 22 °C) δ ppm: 7.86 (d, J = 7.8 Hz, 1H, Ar-H), 7.83 (d, J = 7.8 Hz, 1H, Ar-H), 7.60 – 7.52 (m, 2H, Ar-H), 7.46 – 7.32 (m, 4H, Ar-H), 4.05 (s, 2H, -$CH_2$-), 3.61 – 3.55 (m, 2H, -$CH_2$-), 3.18 – 3.13 (m, 2H, -$CH_2$-). **$^{13}$C NMR** ($CDCl_3$, 100.6 MHz, 22 °C) δ ppm: 195.4, 155.2, 151.9, 148.7, 141.0, 139.7, 133.7, 130.6, 127.4, 127.0, 126.4, 126.1, 126.0, 125.9, 123.7, 33.1, 31.7, 31.0.

### *1.2. Synthesis of monohomotruxene (**MHTX**)*

Under argon atmosphere, a mixture of the 1-indanone dimer (**2**, 1.0 g, 4.1 mmol), commercial 1-tetralone (**3**, 2.4 g, 16.4 mmol), propionic acid (0.53 g, 7.2 mmol) and dried *para*-toluenesulfonic acid (1.4 g, 7.1 mmol) was stirred at 140 °C for 24 hours in *ortho*-dichlorobenzene (5 mL). The reaction flask was kept wrapped in aluminum foil to protect it from light. After cooling down to room temperature, cold methanol (50 mL) was added to the flask and the acid was neutralized with excess 10% aqueous NaOH solution. The resulting precipitate was collected by filtration and washed with additional methanol (20 mL). The light-yellow remaining solid was initially purified by silica gel column chromatography (eluent: 10% DCM in petroleum ether). A second purification by gel permeation chromatography (GPC), using chloroform as the eluent (HPLC isocratic standard, stabilized with ethanol), was necessary to separate **MHTX** from impurities of similar

polarity and solubility[4]. The GPC-purified chloroform solution was concentrated to 10 mL and the product was precipitated by adding methanol (50 mL). The solid was collected by filtration, washed with methanol (10 mL) and recrystallized from acetone.

**Yield**: 0.57 g (356.2 g mol$^{-1}$, 1.6 mmol, 39%) of a white solid. $R_f$ = 0.5 (10% DCM in PE); **m.p**.: >300 °C; **$^1$H NMR** ($CDCl_3$, 400 MHz, 22 °C) δ ppm: 8.05 (d, $J$ = 7.7 Hz, 1H, Ar-H), 8.04 (d, $J$ = 7.7 Hz, 1H, Ar-H), 7.95 (d, $J$ = 7.7 Hz, 1H, Ar-H), 7.70 (d, $J$ = 7.3 Hz, 1H, Ar-H), 7.63 (d, $J$ = 7.3 Hz, 1H, Ar-H), 7.49 – 7.27 (m, 7H, Ar-H), 4.37 (s, 2H, -$CH_2$-), 4.30 (s, 2H, -$CH_2$-), 3.49 – 3.41 (m, 2H, -$CH_2$-), 2.93 – 2.85 (m, 2H, -$CH_2$-). **$^{13}$C NMR** ($CDCl_3$, 100.6 MHz, 22 °C) δ ppm: 144.1, 143.8, 142.2, 141.6, 138.85, 138.82, 138.4, 136.9, 136.4, 135.2, 133.1, 131.2, 127.8, 127.0, 126.9, 126.8, 126.6, 126.6, 126.4, 126.2, 125.3, 124.7, 123.5, 121.8, 39.5, 36.6, 29.5, 26.2. **Elemental analysis** calcd (%) for $C_{28}H_{20}$: C 94.34%; H 5.66%; found: C 93.98%; H 5.55%. **HRMS** (MALDI) m/z: $[M]^{+\cdot}$ calcd for $C_{28}H_{20}$: 356.1560; found: 356.1587.

*1.3. Optimization of reaction conditions for the synthesis of **MHTX**.*

The reaction proceeded best in *ortho*-dichlorobenzene (ODCB) as a solvent for 24 h at 140 °C, due to its high polarity, polarizability, and boiling point. Extended reaction times (48 h) did not contribute significantly to increasing the reaction yield, whereas higher temperatures (180 °C) promoted a reduction in yield, possibly due to the partial evaporation of propionic acid (boiling point = 141.2 °C), which is proposed to be the direct catalyst after protonation by PTSA[5]. Furthermore, higher catalyst concentrations proved detrimental, likely by promoting over-protonation and excessive enol formation of the ketone substrates.

**Table S1.** Optimization of reaction conditions for the synthesis of **MHTX**.

| **Entry** | **Catalysts** / equiv.[a] | **1-tetralone** / equiv.[b] | **Solvent**[c] | **Temperature** / °C | **Time** / h | **Yield** / %[d] |
|---|---|---|---|---|---|---|
| **1** | 1 | 4 | ODCB | 140 | 24 | 10 |
| **2** | 1.75 | 4 | ODCB | 140 | 24 | 39 |
| **3** | 3 | 4 | ODCB | 140 | 24 | 5 |
| **4** | 1.75 | 2 | ODCB | 140 | 24 | 15 |
| **5** | 1.75 | 4 | Toluene | 105 | 24 | traces |
| **6** | 1.75 | 4 | ODCB | 140 | 48 | 40 |
| **7** | 1.75 | 4 | ODCB | 180 | 24 | 26 |

[a] Molar equivalents of PTSA and propionic acid, considering 1 equivalent of the dimer.
[b] Molar equivalents of 1-tetralone, considering 1 equivalent of the dimer.
[c] The concentration of the reactions was maintained at 0.7 mol/L related to the dimer.
[d] Yield of the pure product.

*1.4. Synthesis of homotruxene (**HTX**).*

Under anhydrous conditions and argon atmosphere, a solution of 1-tetralone (**3**) (17.6 g, 0.12 mmol) and DABCO (13.6 g, 0.12 mol) in DCM (80 mL, anhydrous) was rapidly added via an addition funnel to a solution of $TiCl_4$ (32 mL, 0.30 mol) in DCM (80 mL, anhydrous). The reaction is exothermic, and immediately turns dark purple, releasing vapors that were collected in a bubbler glassware filled with ODCB. Subsequently, 80 mL of anhydrous DCM was added. The mixture was then sonicated for 2 minutes to break bigger aggregates, and vigorously stirred at room temperature for 3 hours. Afterward, the flask content was slowly poured into ice/water (300 mL), the product was extracted with DCM (2 x 500 mL) and the organic phase was dried over $MgSO_4$. After removal of solvent under vacuum, the remaining dark oil was purified by chromatography column of silica gel (100/400 μm) with a mixture of 10% of DCM in PE as eluent. The yellowish remaining

solid was solubilized in DCM (6 mL) and the product was precipitated by the addition of cold ethanol (150 mL). The product was collected by filtration and washed with methanol (20 mL).

**Yield:** 3.21 g (384.19 g mol$^{-1}$, 8.3 mmol, 21%) of a white solid. $R_f$ = 0.46 (25% DCM in hexane). **m.p.**: > 300 °C. **$^1$H NMR** ($CDCl_3$, 400 MHz, 22 °C) δ ppm: 7.46 (dd, $J$ = 2 Hz, $J$ = 8 Hz, 3H), 7.32 (dd, $J$ = 2 Hz, $J$ = 8 Hz, 3H), 7.28 (dt, $J$ = 2 Hz, $J$ = 8 Hz, 3H), 7.26 (dt, $J$ = 2 Hz, $J$ = 8 Hz, 3H), 3.35 (broad, 3H), 2.94 (broad, 3H), 2.73 (broad, 3H), 2.63 (broad, 3H). **$^{13}$C NMR** ($CDCl_3$, 100.6 MHz, 22 °C) δ ppm: 140.2, 136.1, 135.1, 133.3, 129.1, 126.9, 126.8, 125.7, 30.6, 30.5 [6].

*1.5. Synthesis of truxene (**TX**)*

A mixture of 1-indanone (**1**, 0.4 g, 3 mmol), propionic acid (0.7 g, 9 mmol) and dried *para*-toluenesulfonic acid (1.5 g, 9 mmol) was stirred at 140 °C for 24 hours in *ortho*-dichlorobenzene (5 mL) under argon atmosphere. The reaction flask was kept wrapped in aluminum foil to protect it from light exposure. After cooling down to room temperature, cold methanol (50 mL) was added to the flask and the acid was neutralized with 10% aqueous NaOH solution. The precipitate was collected by filtration and washed with additional methanol (20 mL). The light-yellow remaining solid was initially purified by silica gel column chromatography (eluent: 10% DCM in petroleum ether) and then boiled in toluene, followed by hot filtration to separate the product from the mother liquor.

**Yield**: 0.2 g (342.4 g mol$^{-1}$, 0.6 mmol, 58%) of a light-yellow solid. $R_f$ = 0.53 (25% DCM in hexane) **m.p.**: >300 °C. **$^1$H NMR** ($CDCl_3$, 400 MHz, 22 °C) δ ppm: 7.91 (d, $J$ = 7.4 Hz, 3H, Ar-H), 7.67 (d, $J$ = 7.4 Hz, 3H, Ar-H), 7.48 (t, $J$ = 7.4 Hz, 3H, Ar-H), 7.38 (td, $J$= 7.4 Hz, $J$ = 0.8 Hz, 3H, Ar-H), 4.20 (s, 6H, -$CH_2$-). **$^{13}$C NMR** ($CDCl_3$, 100.6 MHz, 22 °C) δ ppm: 143.8, 141.7, 137.1, 135.3, 126.9, 126.3, 125.1, 121.9, 36.5 [7].

## 2. NMR Spectra

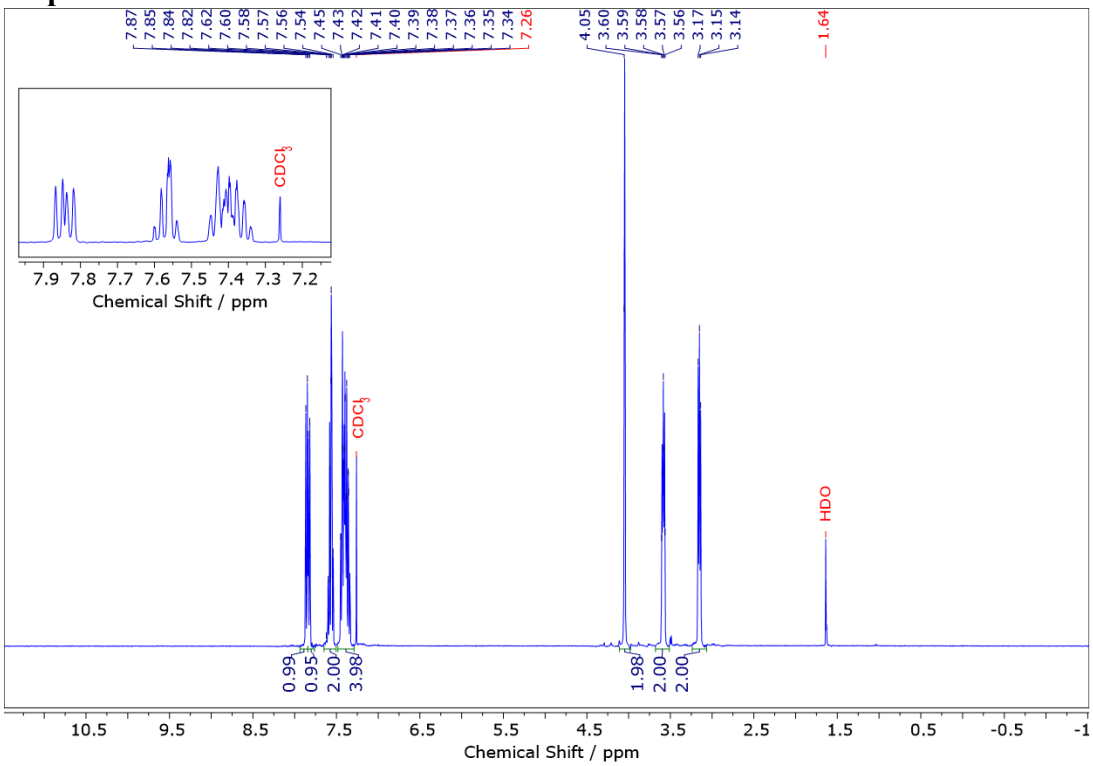


**Figure S1.** $^1$H NMR spectrum of dimer (**2**) in $CDCl_3$ (400 MHz). The inset is the magnification of the aromatic region.

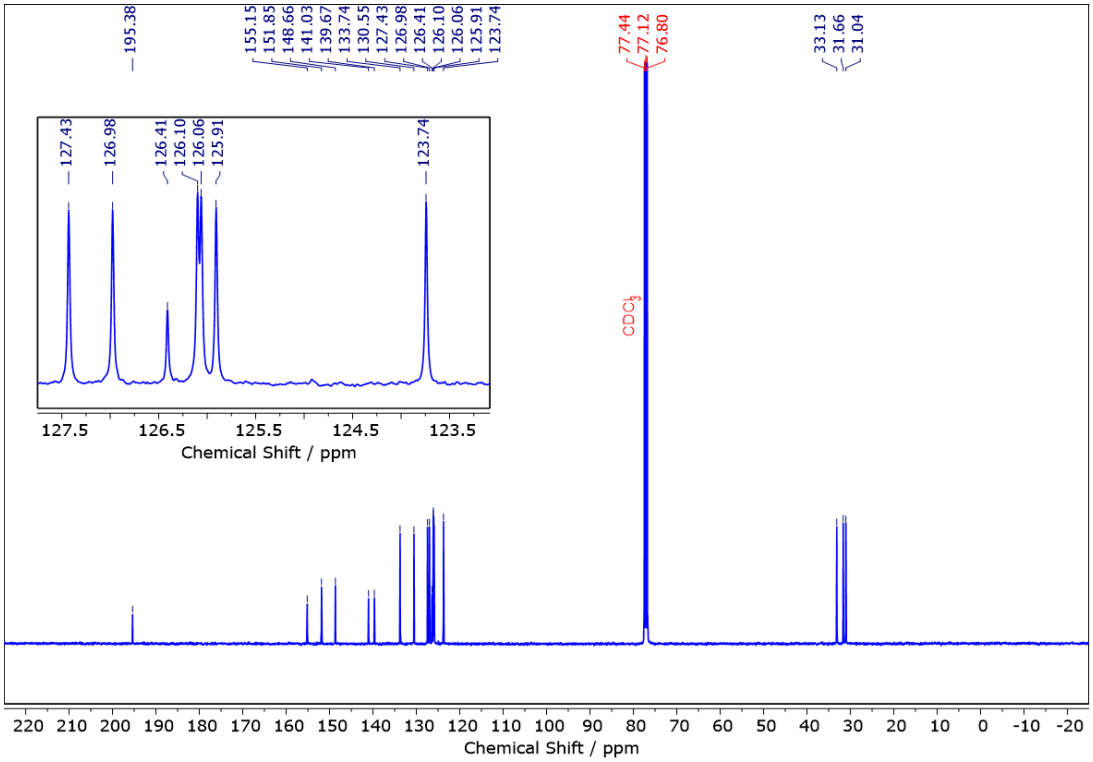


**Figure S2.** $^{13}C$ NMR spectrum of dimer (**2**) in $CDCl_3$ (100.6 MHz). The inset is the magnification of part of the aromatic region.

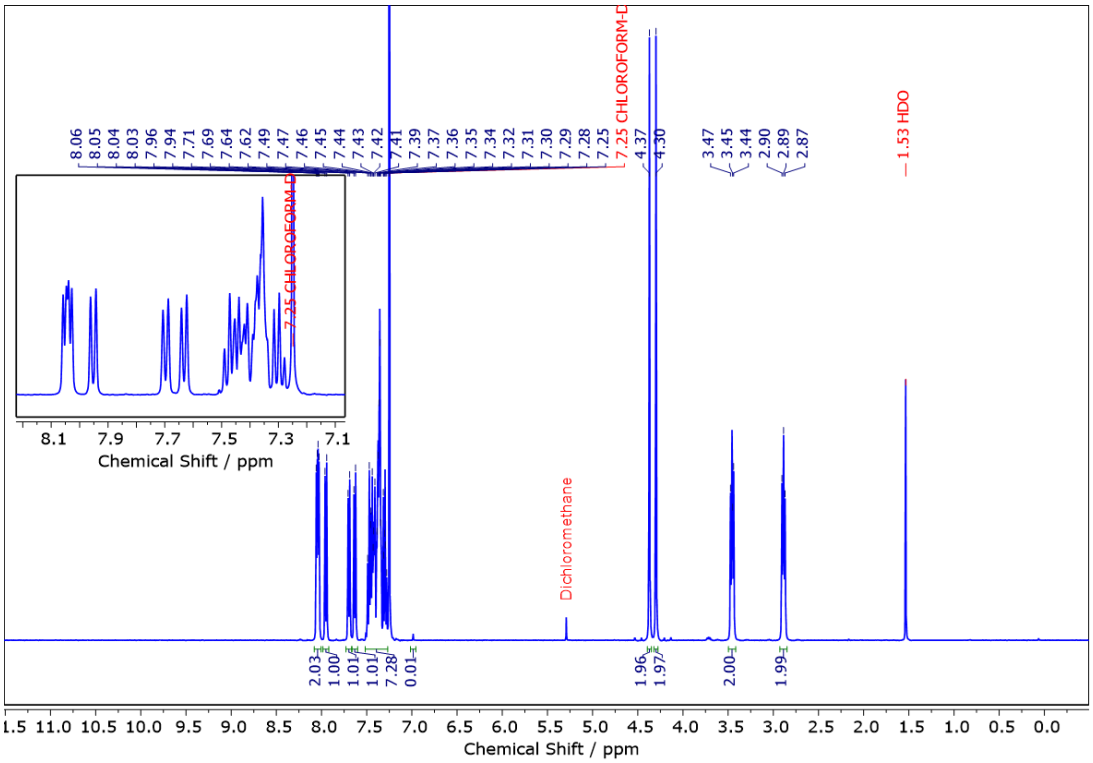


**Figure S3.** $^{1}H$ NMR spectrum of **MHTX** in $CDCl_3$ (400 MHz). The inset is the magnification of the aromatic region.

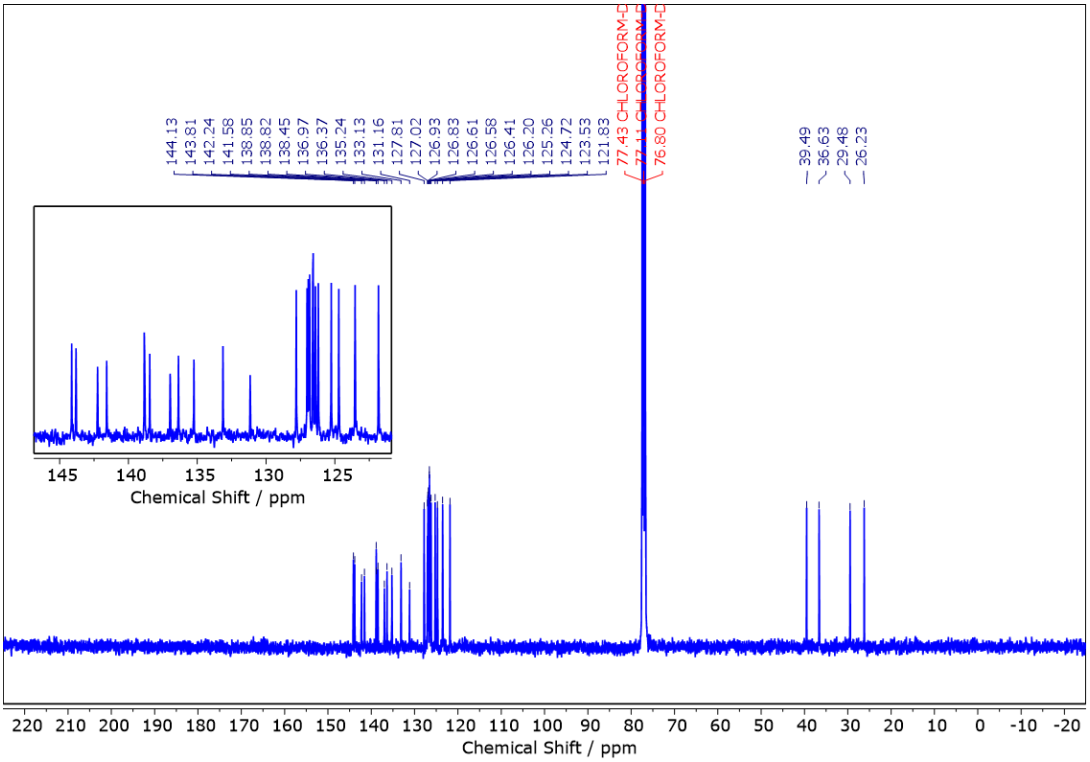


**Figure S4.** $^{13}C$ NMR spectrum of **MHTX** in $CDCl_3$ (100.6 MHz). The inset is the magnification of the aromatic region.

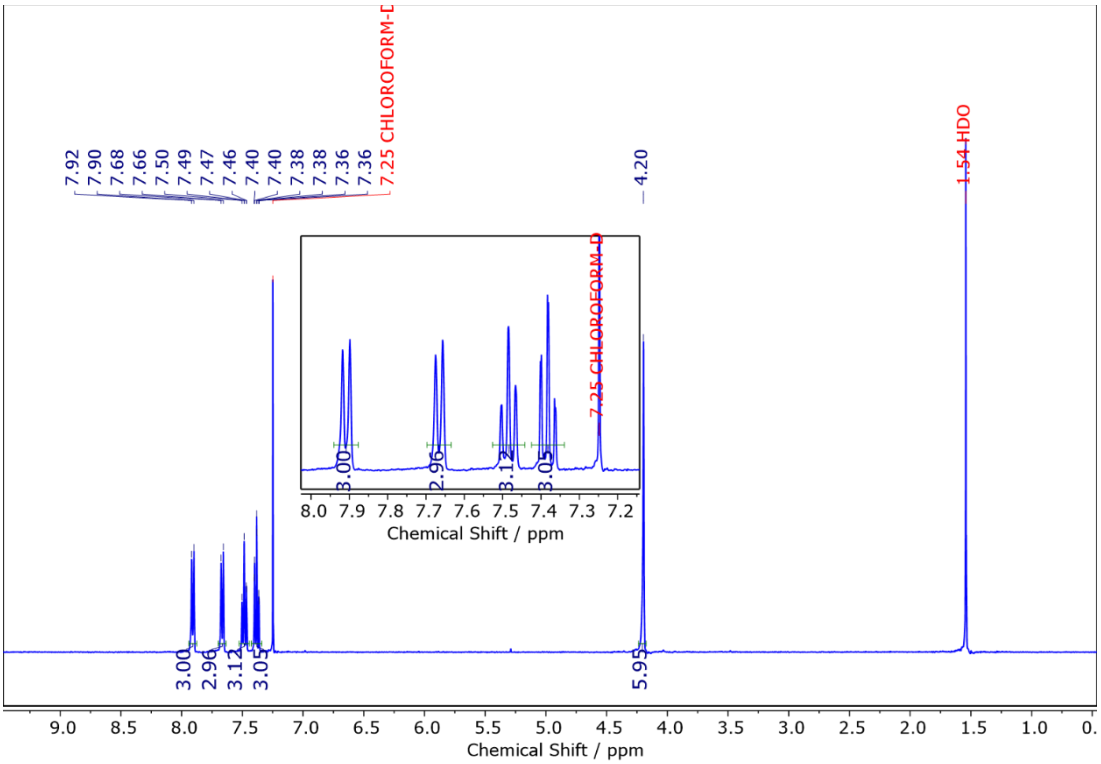


**Figure S5.** $^{1}H$ NMR spectrum of **Truxene** (**TX**) in $CDCl_3$ (400 MHz). The inset is the magnification of the aromatic region.

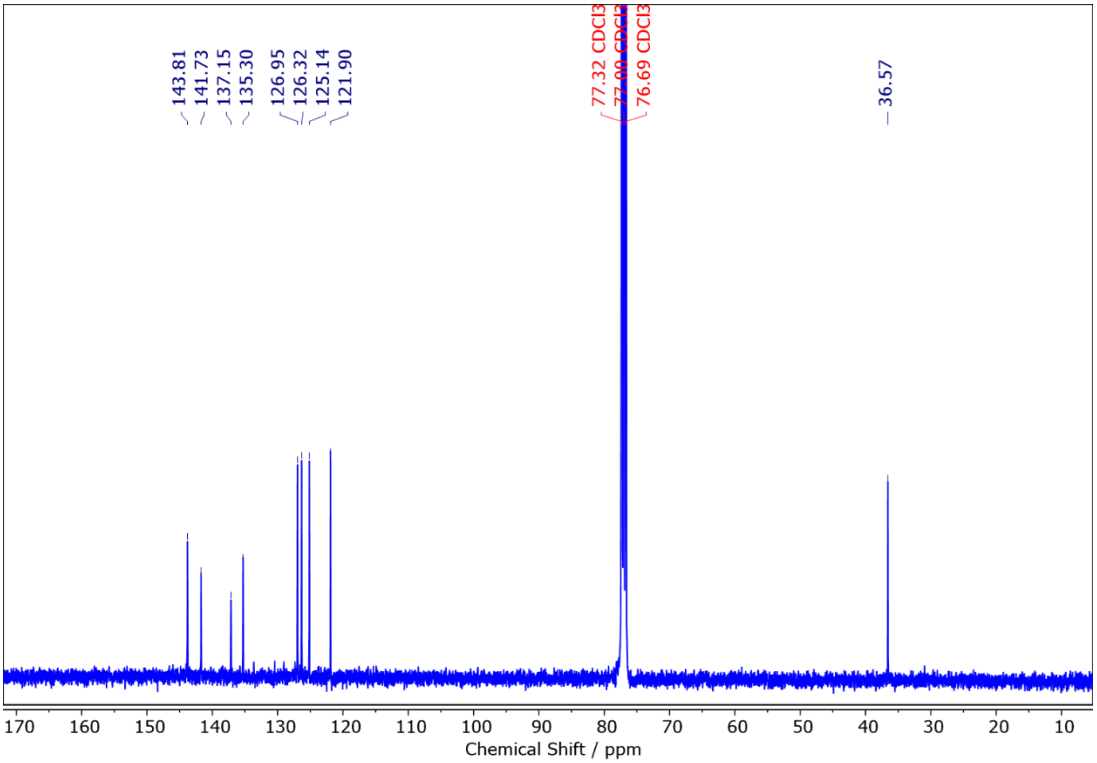


**Figure S6.** $^{13}C$ NMR spectrum of **Truxene** (**TX**) in $CDCl_3$ (100.6 MHz).

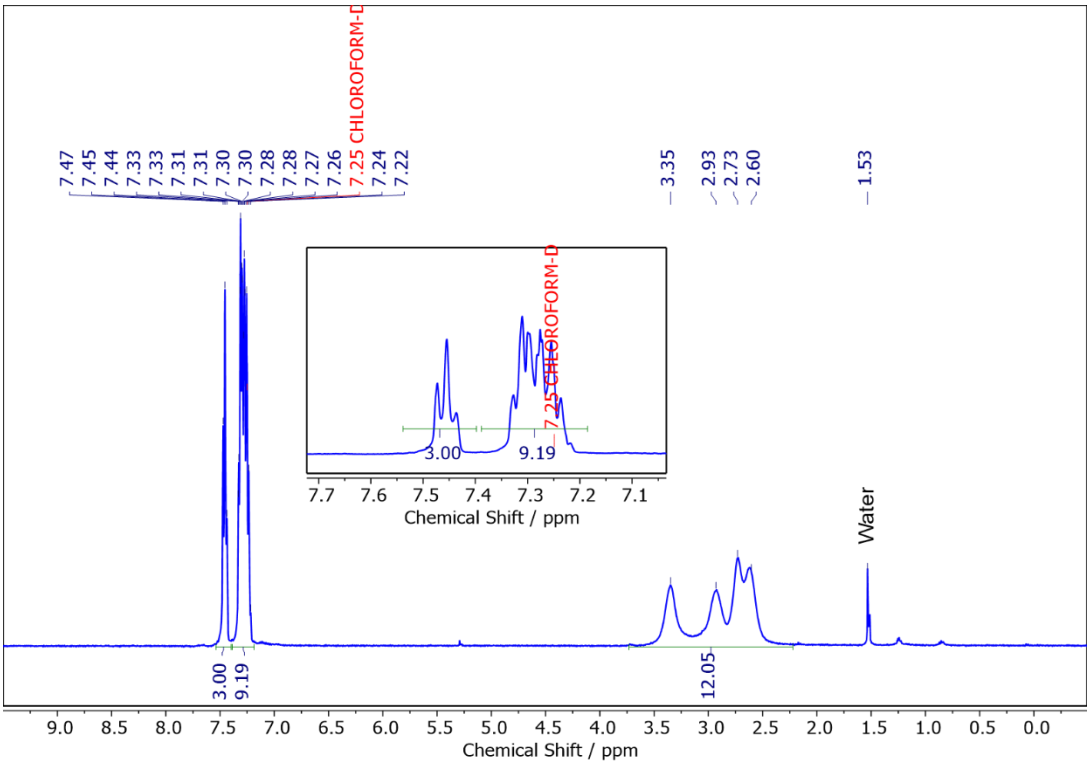


**Figure S7.** $^{1}H$ NMR spectrum of **Homotruxene** (**HTX**) in $CDCl_3$ (400 MHz). The inset is the magnification of the aromatic region.

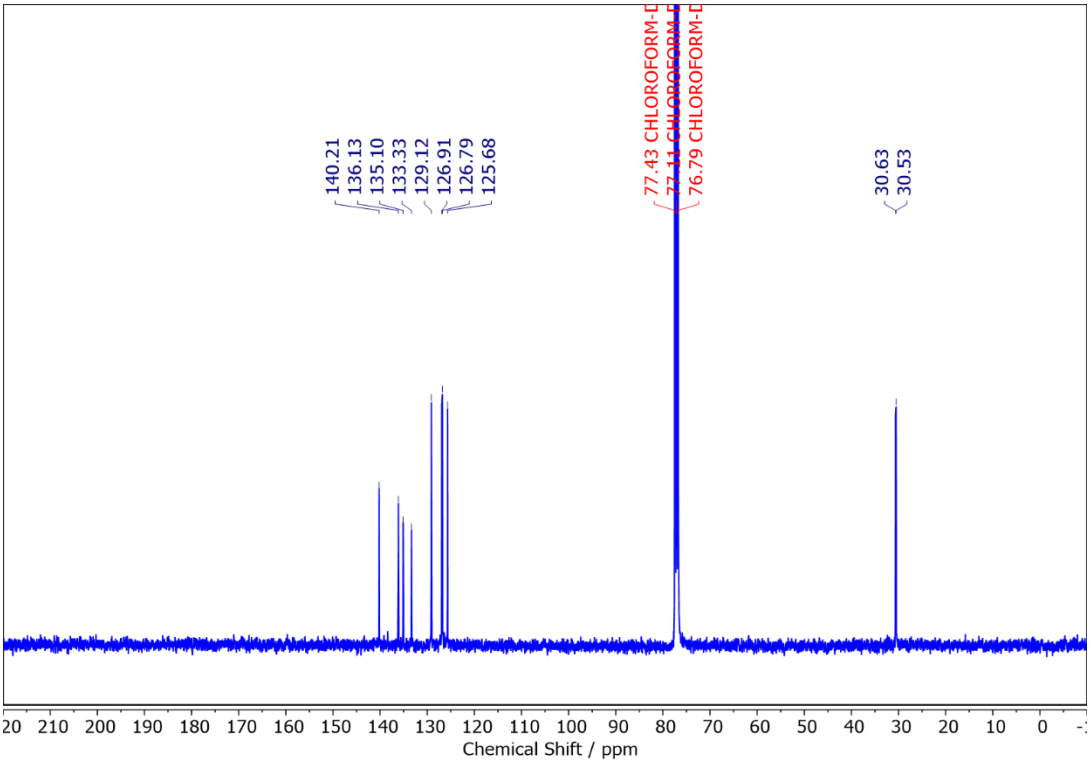


**Figure S8.** $^{13}C$ NMR spectrum of **Homotruxene** (**HTX**) in $CDCl_3$ (100.6 MHz).

## 3. High Resolution Mass Spectrometry

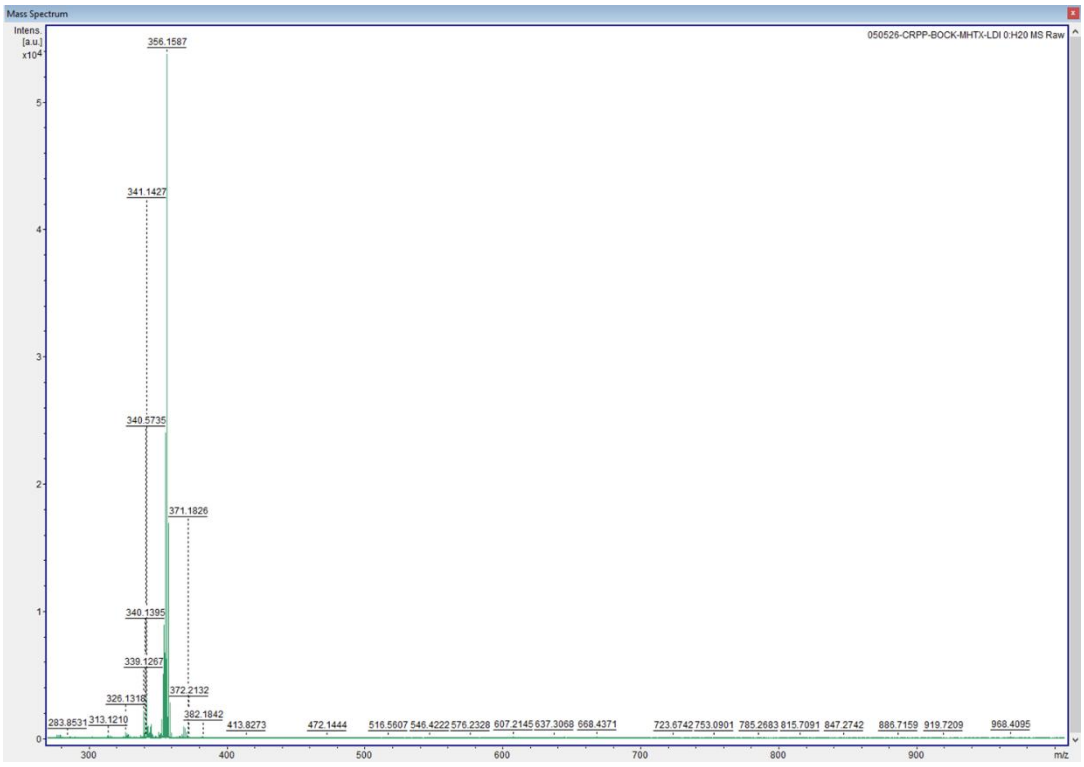


**Figure S9. High Resolution Mass Spectrometry (HRMS) spectrum.** HRMS spectrum of **MHTX** recorded on MALDI-type mass spectrometer equipped with a ToF analyzer via laser desorption ionization (LDI) in positive ion mode. The principal peak observed at m/z = 356.1587 corresponds to the expected molecular ion ($M^+$).

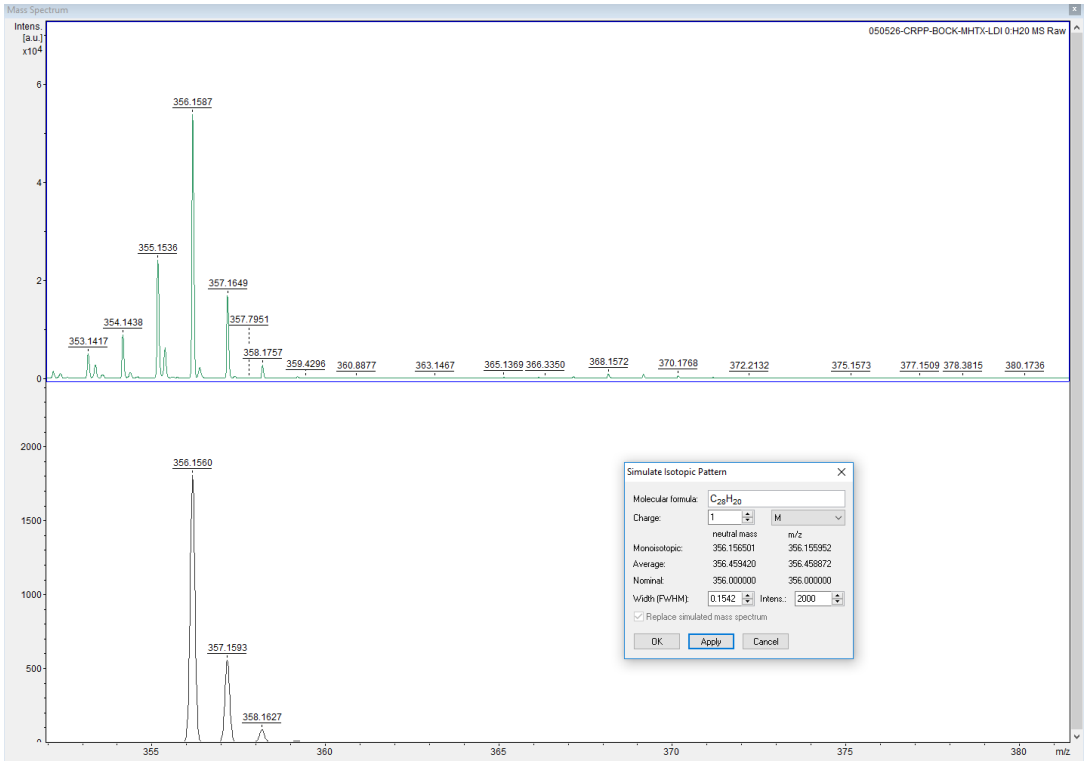


**Figure S10. High-resolution mass spectrometry (HRMS) isotopic pattern confirmation.** Comparison between the experimental (top) and simulated (bottom) HRMS isotopic patterns for **MHTX**. The simulated pattern was generated based on the molecular formula $[C_{28}H_{20}]^+$ (monoisotopic m/z = 356.1560).

## 4. Photophysical Investigations

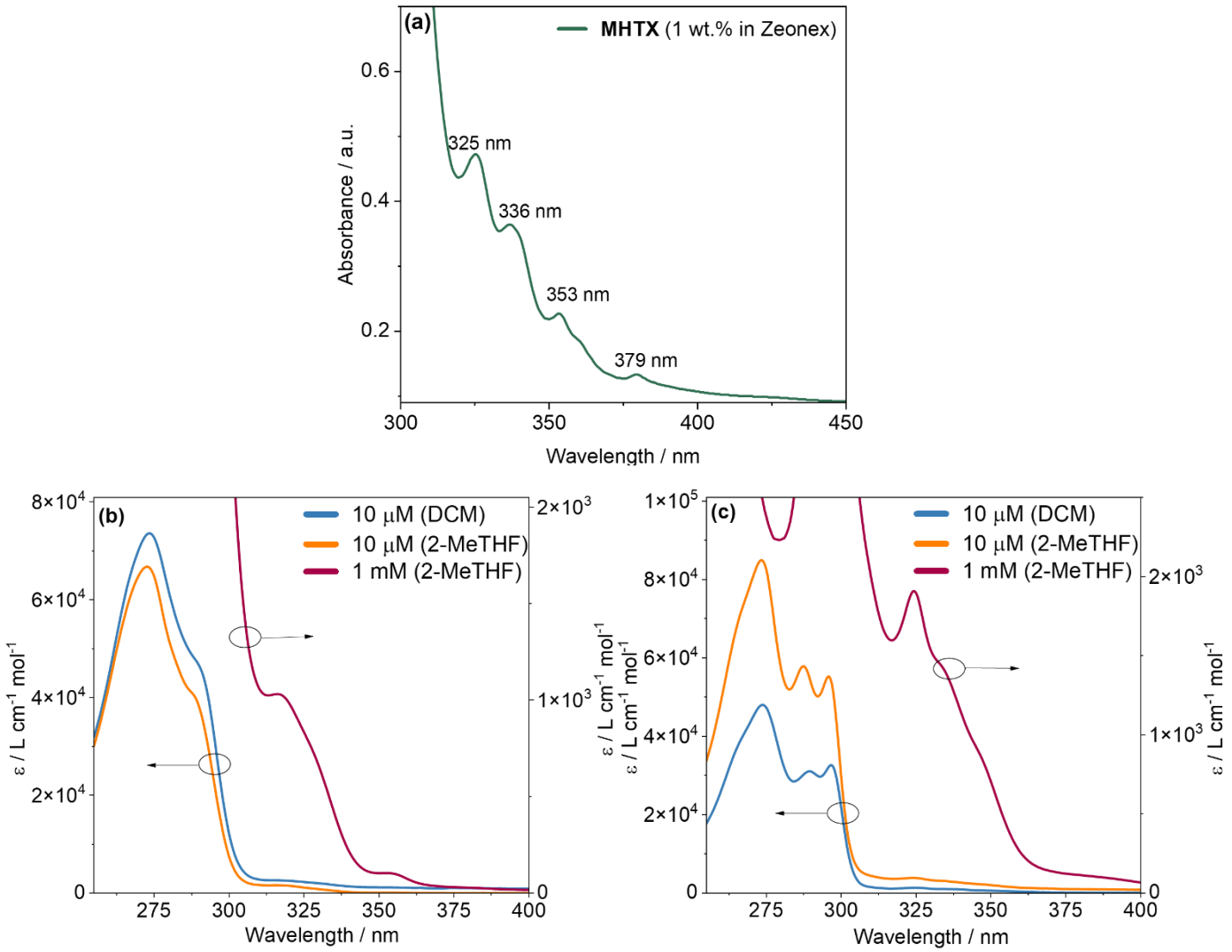


**Figure S11. Steady-state absorption spectra. (a)** Absorption spectrum of **MHTX** in the solid state (1 wt% in Zeonex). Absorption spectra of **(b) HTX** and **(c) TX** recorded as 10 μM solutions in 2-MeTHF (orange) and DCM (blue), alongside a 1 mM solution in 2-MeTHF (dark red).

### *4.1.Singlet quenching*

To elucidate the excited-state kinetics of **MHTX**, time-resolved photoluminescence (TRPL) measurements were performed on diluted solutions (10 μM in 2-MeTHF) under both aerobic and anaerobic conditions (Fig. S12) and the lifetimes are summarized in Table S2. Time-gated measurements at room temperature for both aerated and degassed solutions reveal a broad prompt fluorescence (PF) band, with maxima at 390 and 405 nm upon excitation at 337 and 355 nm (Figure S12a–d). The observed red shift in the $S_2$ emission maxima compared to steady-state measurements is attributed to an internal filter effect, which attenuates the high-energy UV region of the emission band. In the lower-energy spectral region (500–600 nm), a broad and weak emission feature is observed; we attribute this to the radiative decay from the $S_1$ state of higher-order aggregated species.

The prompt fluorescence decay of the $S_2$ state in degassed solution exhibits a long lifetime ($\tau_{PF}$) of 29.7 ns ($\lambda_{Ex}$ = 337 nm; Figure S12e). Similarly, the monomeric $S_1$ decay ($\lambda_{Ex}$ = 355 nm; Figure S12f) possesses a $\tau_{PF}$ of 32.9 ns. Biexponential fitting of the 355 nm excitation data reveals a shorter-lived component attributed to aggregate species, which contributes 5% to the total emission in aerated media and increases to

18% upon deoxygenation. In aerated solutions, the presence of dissolved oxygen effectively quenches both the $S_2$ and $S_1$ monomeric states, reducing their lifetimes by a factor of approximately three, while the lifetime of aggregate species is reduced by a factor of two.

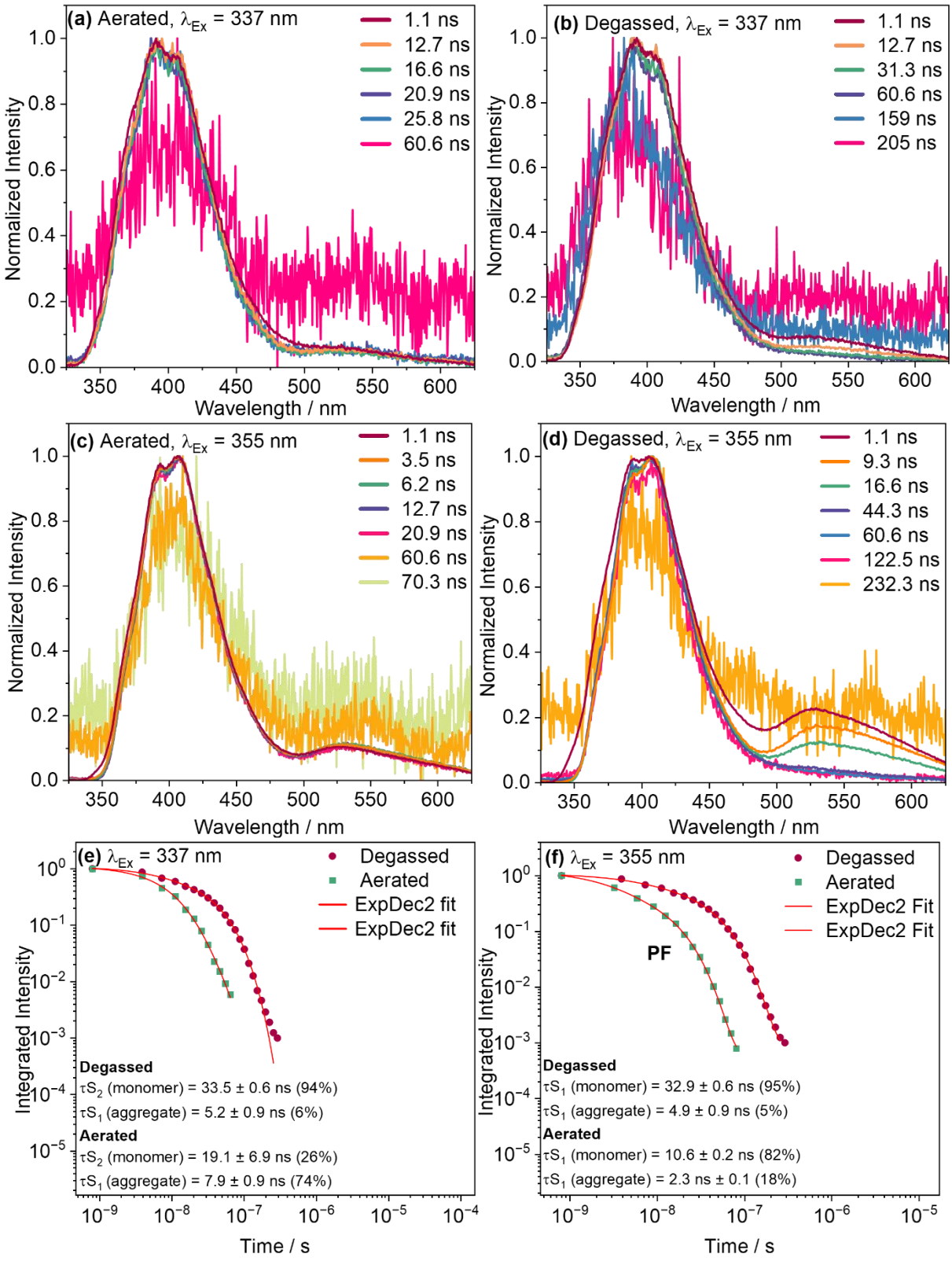


**Figure S12. Time-resolved photoluminescence of MHTX in solution. (a–d)** Time-gated emission spectra of **MHTX** in 2-MeTHF (10 μM) recorded under various atmosphere and excitation conditions: (a and c) Aerated solutions excited at 337 nm and 355 nm, respectively; (b and d) degassed solutions containing dissolved molecular oxygen. **(e–f)** Photoluminescence decay curves obtained from time-gated measurements in 2-MeTHF (10 μM) under degassed (red circles) and aerated (green squares) conditions, recorded upon excitation at (e) 337 nm ($S_2$ state) and (f) 355 nm ($S_1$ state).

To confirm the lifetimes obtained by time-gated experiments, time-correlated single photon counting (TCSPC) measurements were perfomed in dilute solutions in the presence of molecular oxygen by exciting at both the $S_2$ and $S_1$ states (Figure S13). The values obtained ($\tau S_2$ = 11.9 ns) showed good agreement with previous lifetime measurements in aerobic conditions, reflecting the reliability of the results.

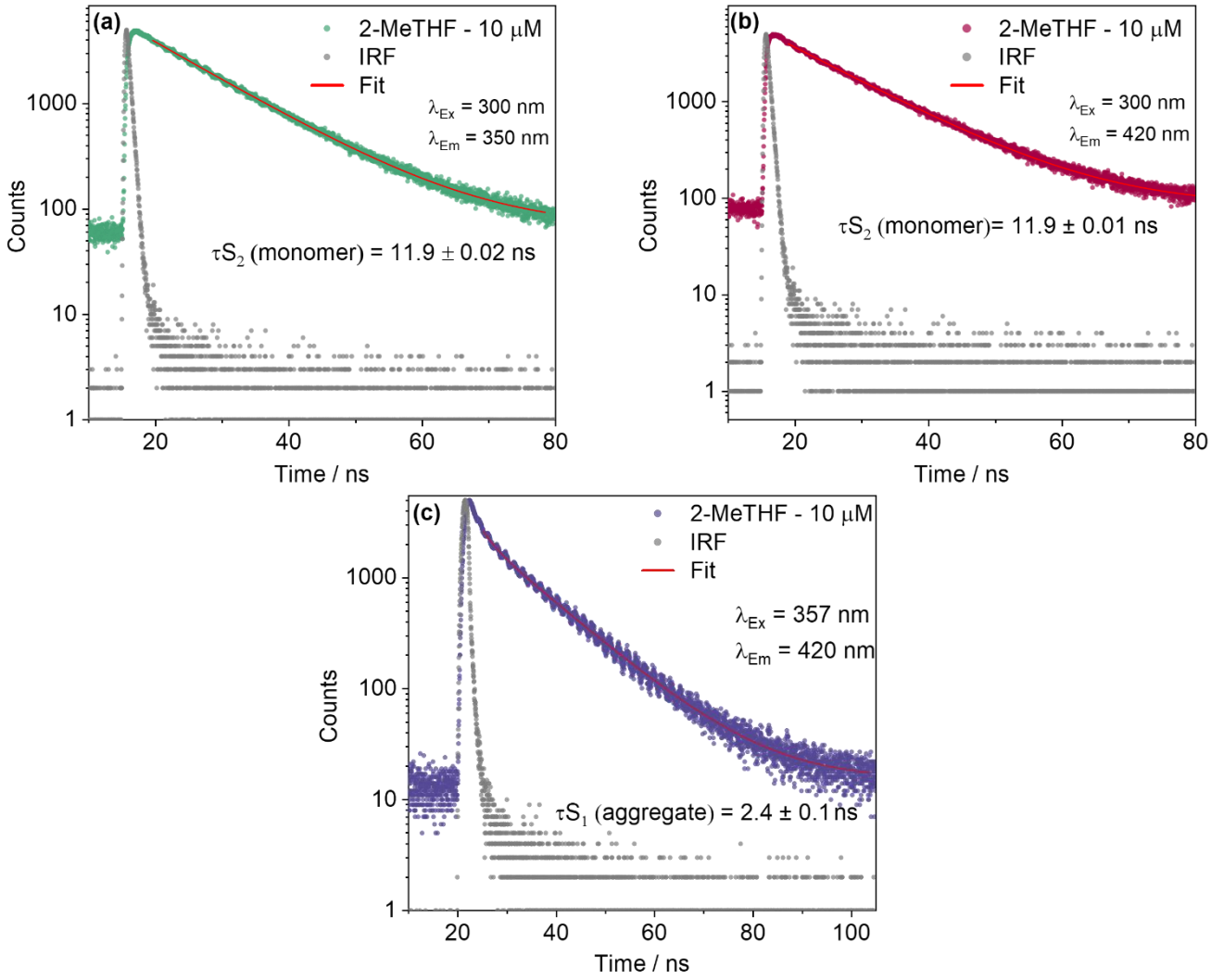


**Figure S13. Decay curves of MHTX in 2-methyltetrahydrofuran (2-MeTHF) solution.** Prompt fluorescence (PF) decay profiles of **MHTX** (10 μM in 2-MeTHF) at room temperature in the presence of molecular oxygen. **(a)** Decay monitored at $\lambda_{Em}$ = 350 nm upon excitation of the S2 state ($\lambda_{Ex}$ = 300 nm). **(b)** Decay monitored at $\lambda_{Em}$ = 420 nm ($\lambda_{Ex}$ = 300 nm). **(c)** Decay profile upon selective excitation of the $S_1$ state ($\lambda_{Ex}$ = 357 nm) monitored at $\lambda_{Em}$ = 420 nm. The red solid lines are numerical fits and gray dots indicate the instrument response function (IRF).

**Table S2.** Summary of fluorescence lifetimes for monomeric and aggregate species of **MHTX** (10 μM) in 2-MeTHF.

| **Conditions** | $\tau S_2$(monomer) / ns[a] | $\tau S_1$(monomer) / ns ($A_1$) [b] | $\tau S_1$(agregate) / ns ($A_2$) [b] |
|---|---|---|---|
| Degassed solution | 29.7 | 32.9 (95%) | 4.9 (5%) |
| Aerated solution | 9.2 | 10.6 (82%) | 2.3 (18%) |

[a] Recorded with $\lambda_{Ex}$ = 337 nm to selectively address the $S_2$ manifold. [b] Recorded with $\lambda_{Ex}$ = 355 nm ($S_1$ excitation); values in parentheses ($A_i$) represent the relative amplitudes (pre-exponential factors) obtained from biexponential fitting of the decay curves.

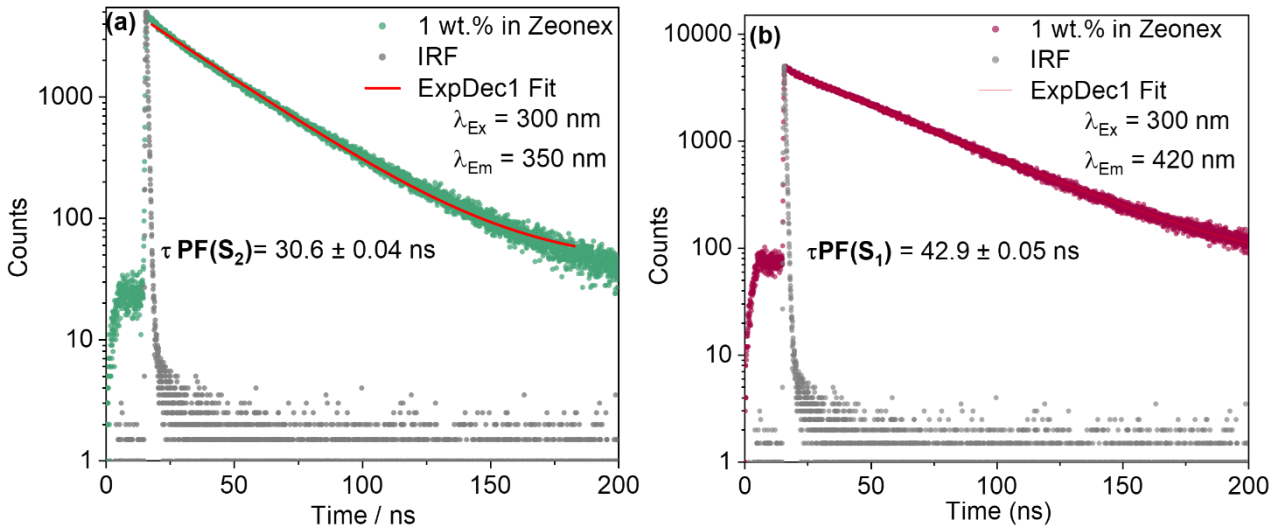


**Figure S14. Decay curves of MHTX doped into guest-host film.** Excited-state kinetics in the solid state. Time-correlated single photon counting (TCSPC) decay curves of **MHTX** (1 wt.% in Zeonex) in the presence of oxygen (T = 298 K). **(a)** Decay of the monomeric anti-Kasha $S_2$ emission recorded at $\lambda_{Em}$ = 350 nm. **(b)** Decay of the $S_1$ emission recorded at $\lambda_{Em}$ = 420 nm. Both states were addressed upon excitation at $\lambda_{Ex}$ = 300 nm. Gray scatter points represent the instrumental response function (IRF).

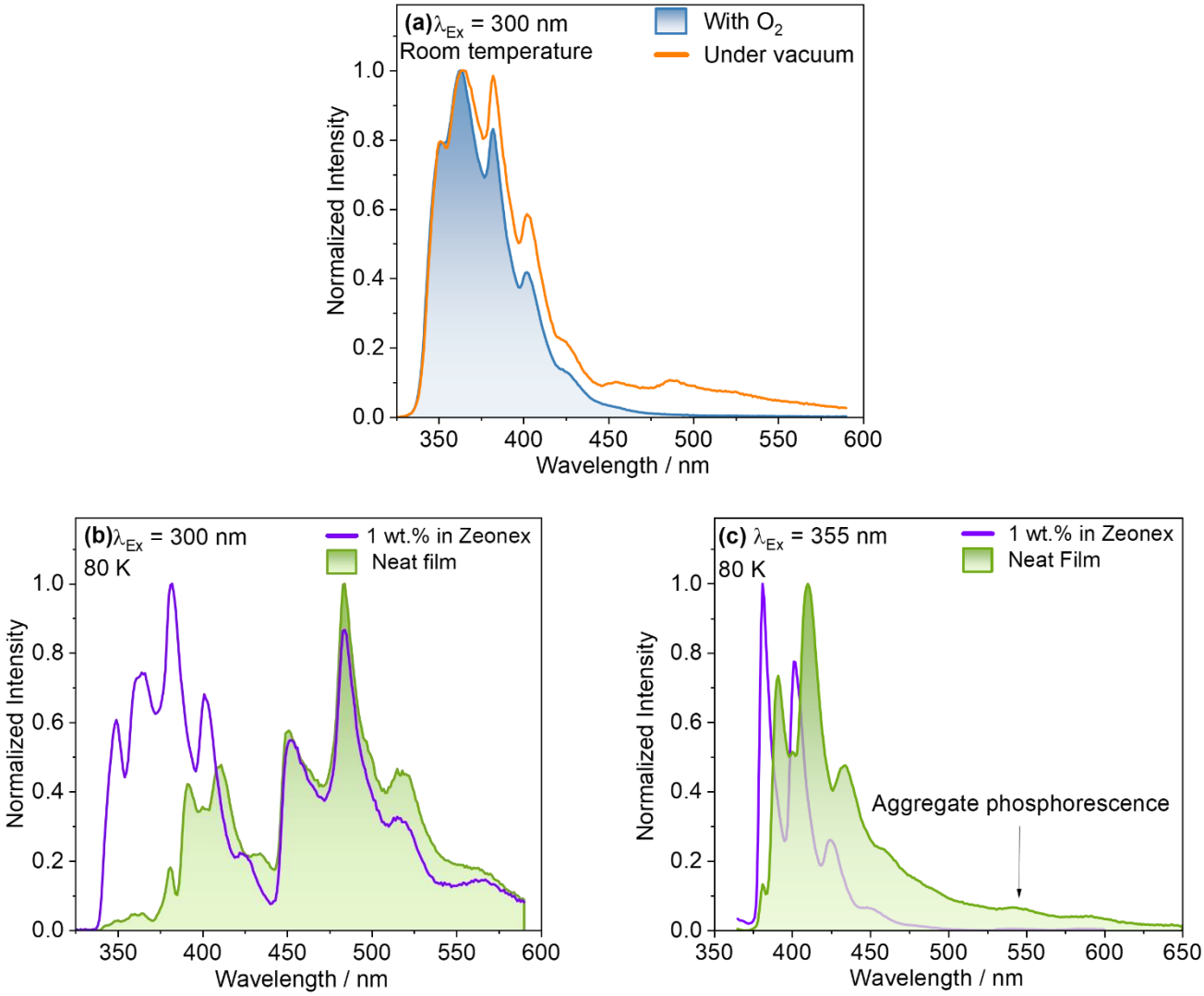


**Figure S15. Behavior of MHTX in solid-state.** Steady-state emission spectra of **MHTX** in the solid state under varying conditions. (a) Emission at room temperature (298 K) in 1-wt.%-in-Zeonex drop-cast film, under vacuum (orange line) and in air (shaded blue) with excitation at $\lambda_{Ex}$ = 300 nm. (b and c) Low-temperature (80 K) emission comparing a dilute matrix (1 wt.% in Zeonex, purple

line) to a neat film (shaded green) upon excitation at $\lambda_{Ex}$ = 300 nm (b); and $\lambda_{Ex}$ = 355 nm (c). The arrow in panel (c) indicates the emergence of a broad aggregate phosphorescence band at longer wavelengths in the neat film.

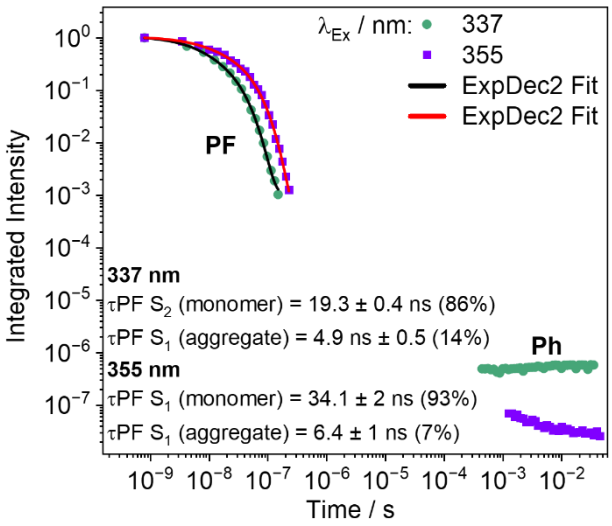


**Figure S16.** Integrated photoluminescence intensity as a function of time obtained from time-gated emission spectra at 80 K (Figure 3e and f) upon excitation at: 337 nm, green circles, 0.5 wt.% in Zeonex; and 355 nm, purple squares, 0.1 wt.% in Zeonex.

### *4.2. Antisolvent experiment*

In mixtures with low to moderate water content (1–60%), the $S_2$ and $S_1$ emission intensity progressively increases with gradual water addition (Extended Figures 2a and b, respectively). This enhancement is attributed to the formation of a more viscous microenvironment with reduced oxygen solubility, that effectively suppresses the diffusion of molecular oxygen, thereby mitigating singlet quenching in solution ($\eta_{THF}$(25 °C) = 0.477 mPa $s^{-1}$ [8]; $\eta_{water}$(25 °C) = 0.890 mPa $s^{-1}$ [9]). To validate this assignment, key mixtures were analyzed after purging the solution with argon (Extended Figures 2c), showing no significant change in emission intensity for the 0–60% fractions under deoxygenated conditions. This stability suggests that up to 60%, the strong THF-**MHTX** interaction forms a protective solvation shell, effectively hindering molecular aggregation by water addition. At a critical water fraction of 70%, the monomeric $S_2$ emission intensity decreases sharply, concurrent with the emergence of a distinct, vibronically resolved fluorescence band (Extended Figures 2a). This new feature exhibits a 4 nm (0.03 eV) bathochromic shift relative to the monomeric $S_1$ emission (Extended Figures 2b), signaling the onset of formation of a weak intermolecular coupling dimer, herein called "loose dimer" that emits exclusively from its $S_1$ state. Upon further increasing the water content above 80%, the system enters a fully aggregated state that accompanies the complete quenching of both $S_2$ and $S_1$ monomeric fluorescence, as the emissive profile becomes dominated by the loose dimer emission.

To investigate their absorption characteristics, excitation spectra were collected at various emission wavelengths during the antisolvent experiment. The excitation spectra monitored at 360 nm (Figure S17a) exhibited a substantial decrease in intensity at 70% water content, followed by a complete quenching at fractions above 80%. These observations confirm two key points: first, the higher-energy emission band is solely related to monomeric species, and second, the system reaches a state of complete aggregation above 80% water content. When collected at 400 nm, where both species emit from their $S_1$ state, (Figure S17b) a slight red-shift is observed above 80% water fraction, similar to the red-shift obtained in the emission spectra (see Extended Figures 2b). The shifted excitation spectrum develops new excitation bands at wavelengths

longer than 365 nm, attributable exclusively to aggregate species. Finally, when monitored at 450 nm, a region specific to aggregate emission (Figure S17c), the excitation intensity increased substantially with higher water content, confirming that emission at this wavelength originates directly from the aggregates, and that their absorption profile is similar to monomeric species.

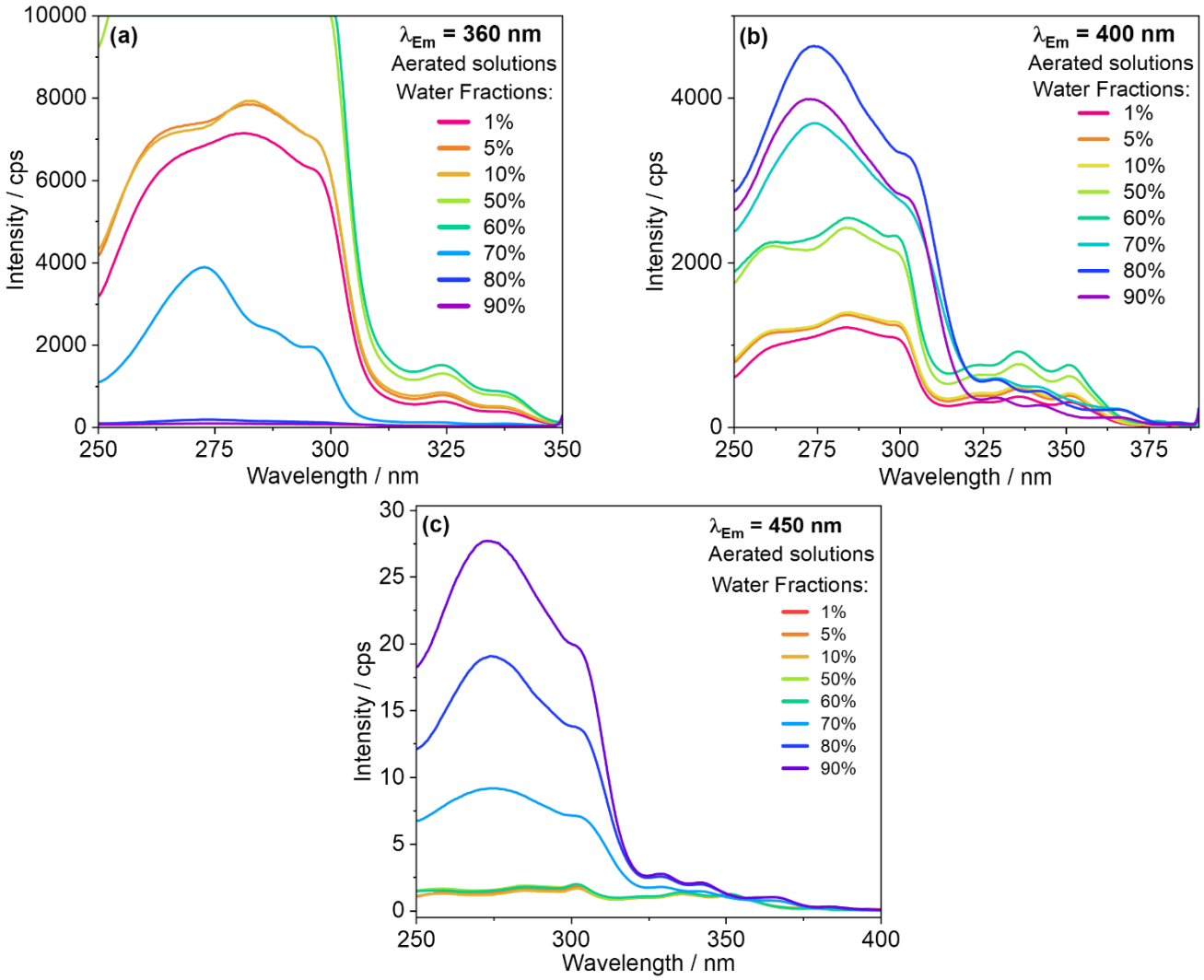


**Figure S17. Effect of water content of the photophysics of MHTX.** Steady-state photoluminescence and excitation spectra of **MHTX** in THF/water mixtures with varying water fractions ($f_w$) maintaining a constant total concentration of 20 μM. **(c)** Emission spectra ($\lambda_{Ex}$ = 300 nm) in degassed solutions, highlighting the intensity enhancement upon oxygen removal. (d–f) Excitation spectra monitored at **(d)** 360 nm, **(e)** 400 nm, and **(f)** 450 nm. The emergence of new features at $f_w$ = 70% in panel **(f)** confirms the formation of weakly coupled aggregates.

*4.3.Room-temperature time-resolved photoluminescence in solid-state films*

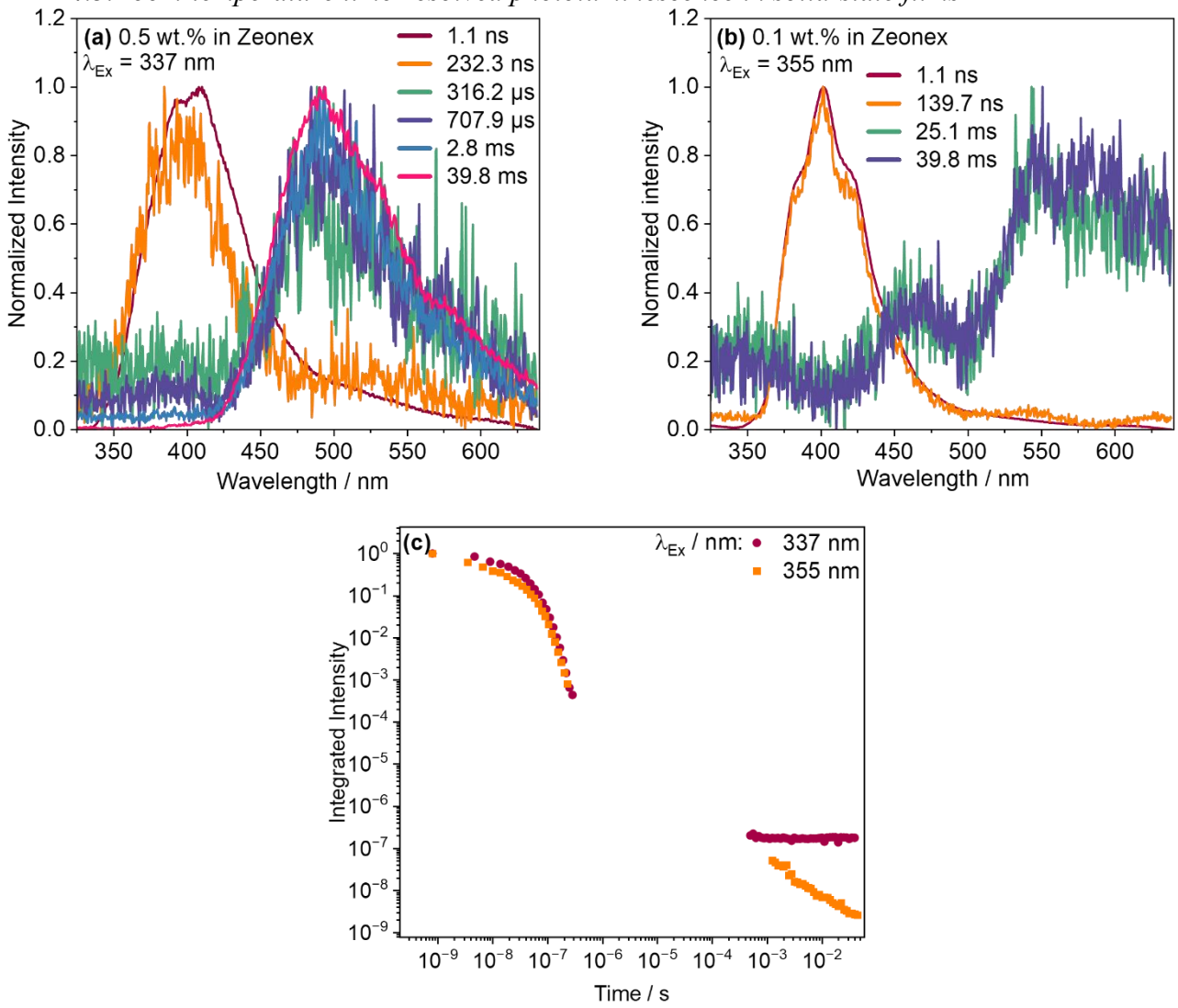


**Figure S18. Time-resolved photoluminescence of MHTX doped into guest-host film.** Room-temperature time-resolved photoluminescence in solid-state films. (a–b) Time-gated emission spectra of **MHTX** in Zeonex films at room temperature (298 K), recorded at indicated time delays following excitation at **(a)** 337 nm (0.5 wt.% film) and **(b)** 355 nm (0.1 wt.% film). **(c)** Integrated photoluminescence intensity as a function of time for both excitation wavelengths (337 nm, dark red circles; 355 nm, orange squares).

*4.4.Low-temperature time-resolved photoluminescence in dilute solution*

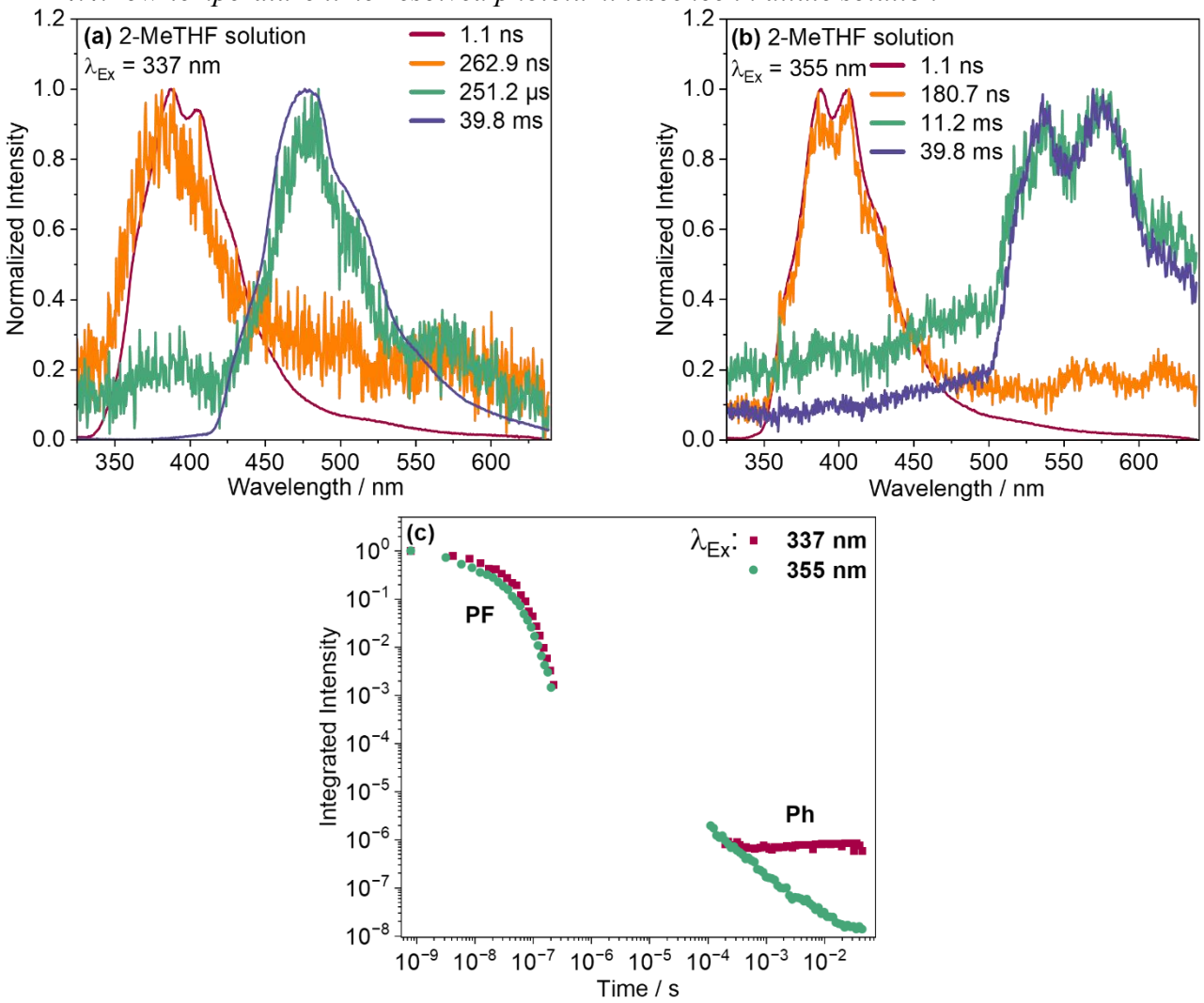


**Figure S19. Low-temperature time-resolved photoluminescence in frozen solution. (a–b)** Time-gated emission spectra of **MHTX** (10 µM in 2-MeTHF) at 80 K recorded at various delay times following excitation at **(a)** 337 nm and **(b)** 355 nm. **(c)** Integrated photoluminescence intensity as a function of time (decay profile) for both excitation wavelengths (337 nm, dark red squares; 355 nm, green circles).

*4.5.Time-resolved photoluminescence of MHTX as a neat film*

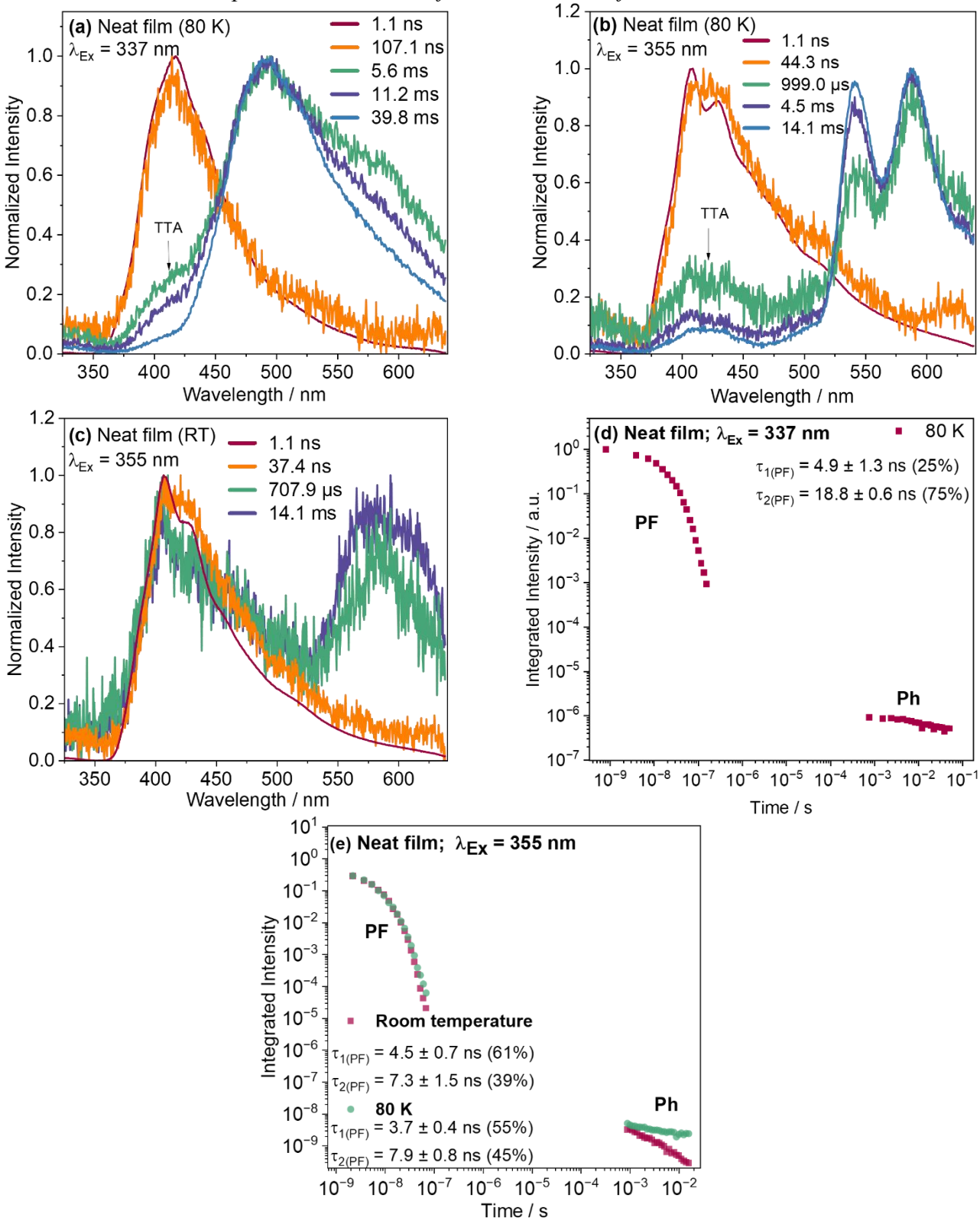


**Figure S20. Time-resolved photoluminescence of MHTX in neat film. (a–b)** Time-gated emission spectra of a neat film at 80 K upon excitation at (a) 337 nm and (b) 355 nm. Arrows indicate the contribution of triplet-triplet annihilation (TTA). **(c)** Time-gated emission of a neat film at room temperature (298 K) following 355 nm excitation. (d–e) Integrated photoluminescence intensity decays for the neat film upon excitation at: **(d)** 337 nm and **(e)** 355 nm. The later measured at both room temperature (blue squares) and 80 K (green circles).

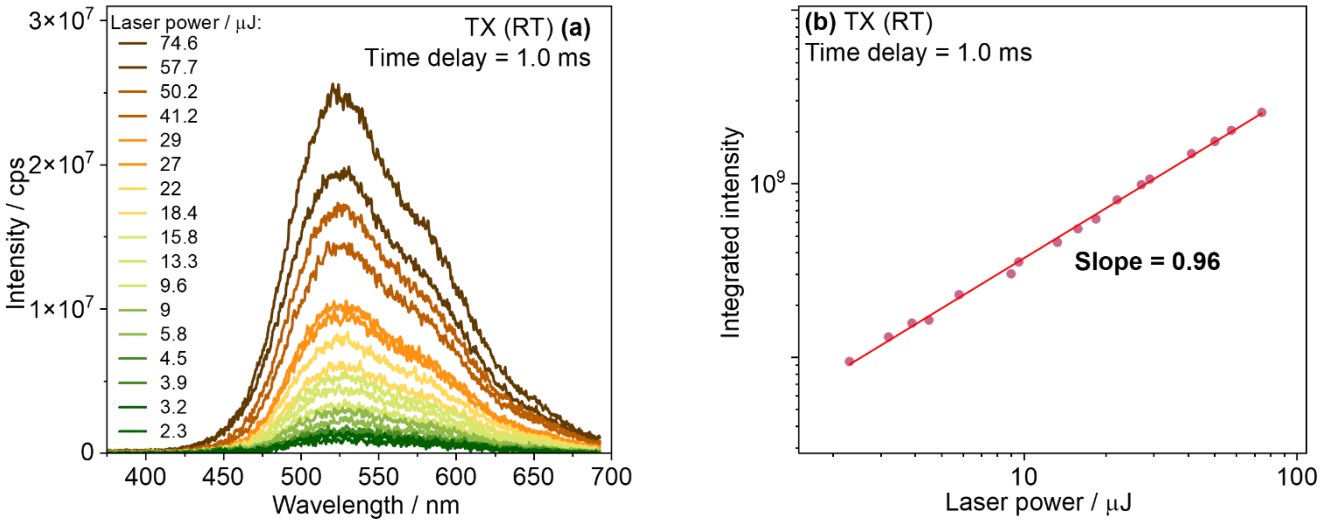


**Figure S21. Investigation of long-lived emission of truxene.** Time-resolved photoluminescence spectra (left) and power-dependent plot (right) of truxene **(TX)** under vacuum ($\lambda_{Ex}$ = 337 nm) at 298 K for a 1 wt.% Zeonex drop-cast film.

## 5. DFT Calculations

**Table S3.** Franck-Condon excited states at the $S_0$ optimized structure. Major configurations are shown where CI coefficients exceed 0.3. If no configuration meets this threshold, those with coefficients greater than 0.24 are presented.

| State | Excitation Energy | | Oscillator | Major Configurations |
|---|---|---|---|---|
| | /eV | /nm | Strength | (CI Coefficients) |
| $T_1$ | 3.071 | 403.8 | - | HO→LU+1 (-0.3464), HO→LU (0.4746) |
| $T_2$ | 3.438 | 360.6 | - | HO-1→LU (-0.3633), HO→LU+1 (0.3526) |
| $T_3$ | 3.451 | 359.3 | - | HO-1→LU (0.3233), HO-1→LU+1 (0.4065), HO→LU (0.3526) |
| $T_4$ | 3.775 | 328.4 | - | HO-1→LU (0.4017), HO→LU+1 (0.4376) |
| $S_1$ | 3.907 | 317.4 | 0.0012 | HO-1→LU (0.4289), HO→LU+1 (0.4515) |
| $T_5$ | 3.984 | 311.2 | - | HO-2→LU (0.3721), HO→LU+2 (0.3093) |
| $T_6$ | 4.034 | 307.3 | - | HO-2→LU+1 (0.3140), HO-1→LU+2 (-0.3009) |
| $T_7$ | 4.244 | 292.1 | - | HO-5→LU+3 (-0.2391), HO-4→LU+4 (0.2416) |
| $T_8$ | 4.296 | 288.6 | - | HO→LU+3 (0.4260) |
| $T_9$ | 4.338 | 285.8 | - | HO-3→LU (0.2972), HO-1→LU+3 (-0.2497), HO-1→LU+5 (0.2404) |
| $T_{10}$ | 4.358 | 284.5 | - | HO-4→LU (0.2875), HO-3→LU+1 (-0.2846) |
| $S_2$ | 4.413 | 281.0 | 0.3503 | HO-1→LU (-0.3844), HO→LU (0.5575) |
| $T_{11}$ | 4.446 | 278.9 | - | HO-4→LU+3 (0.3213) |
| $S_3$ | 4.475 | 277.0 | 0.6826 | HO-1→LU (-0.3653), HO→LU+1 (0.4644) |
| $T_{12}$ | 4.476 | 277.0 | - | HO-3→LU+5 (0.2794), HO-2→LU+1 (-0.2518) |
| $S_4$ | 4.553 | 272.3 | 0.4803 | HO-1→LU+1 (0.6351) |

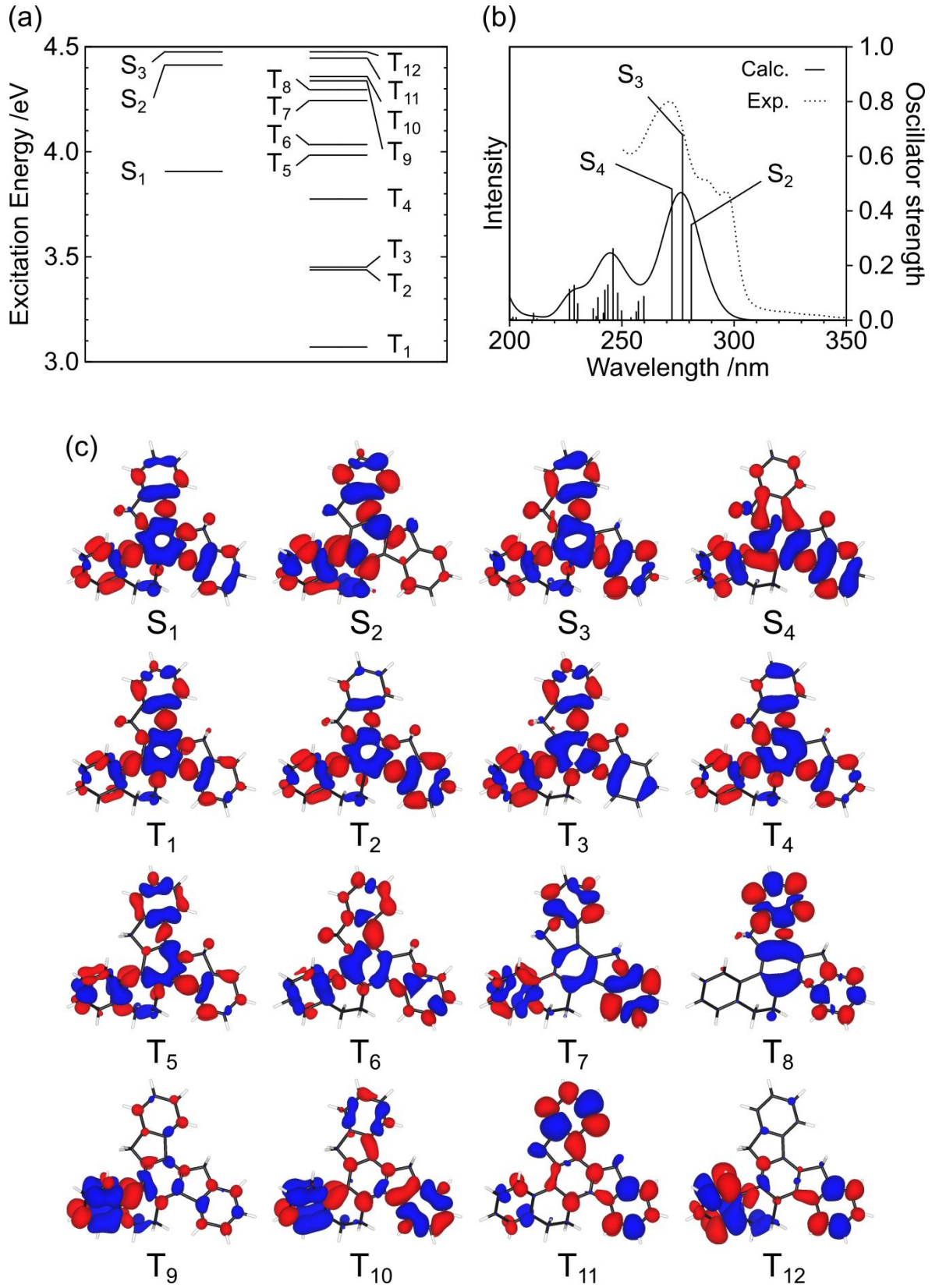


**Figure S22. Theoretical calculations of MHTX at ground state.** (a) Energy levels of the Franck-Condon excited states at the $S_0$ optimized structure. (b) Calculated UV/Vis spectrum obtained by broadening the oscillator strengths using a Gaussian function with a linewidth of 1000 $cm^{-1}$. (c) Electron density differences for $S_n$-$S_0$ and $T_n$-$T_0$ at the $S_0$ optimized structure (isosurface value: $5.0 \times 10^{-4}$ a.u.). Red and blue regions indicate positive and negative values, respectively.

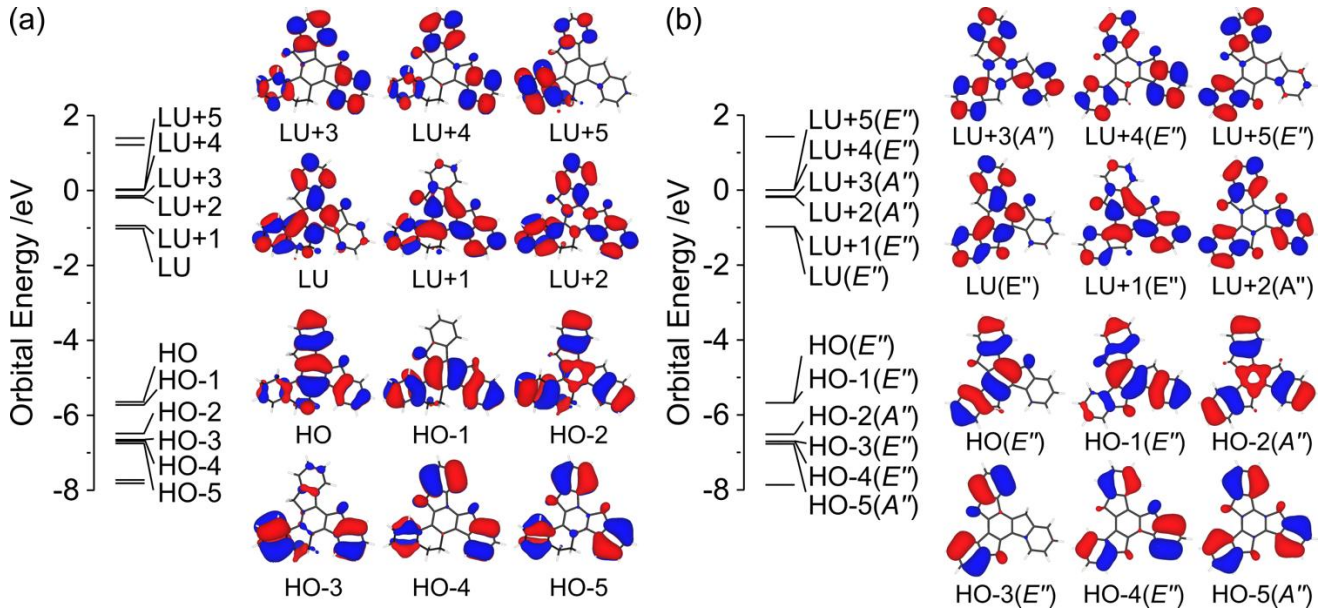


**Figure S23. Calculated energy levels and molecular orbitals for MHTX and truxene.** Orbital energy levels and molecular orbitals (isosurface value: $2.0 \times 10^{-2}$ a.u.) at the $S_0$ optimized structure for (a) **MHTX** ($C_1$ symmetry) and (b) **TX** ($C_{3h}$ symmetry).

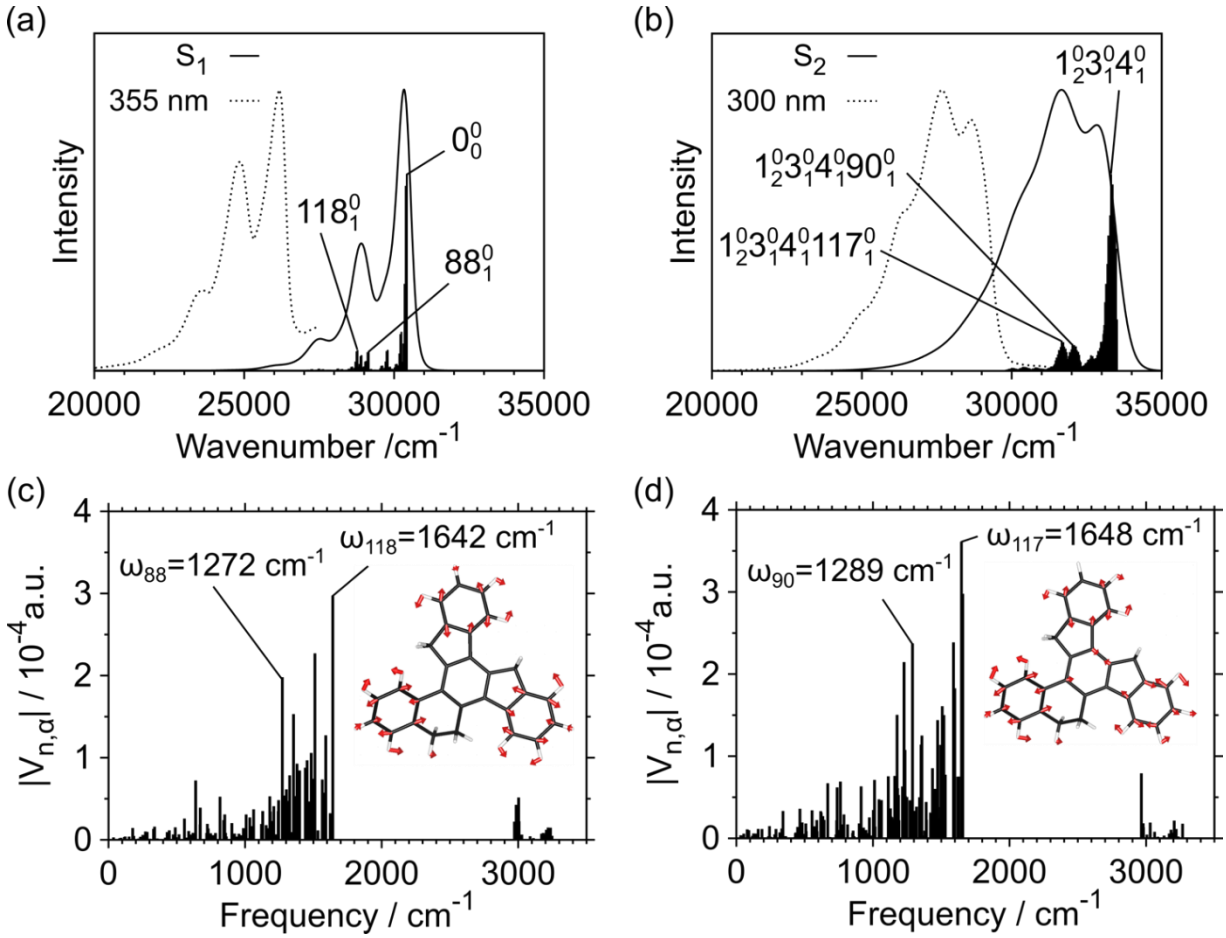


**Figure S24. Calculated spectra of MHTX.** Calculated fluorescence spectra from (a) $S_1$ and (b) $S_2$ at $T$ =300 K (solid lines), compared with the experimental spectra (dotted lines, Figure 2b). The density of final vibronic states is expressed using a Gaussian function with a linewidth of 100 $cm^{-1}$. Vertical lines represent the Franck-Condon factor. Specifically, $0_0^0$ represents the Franck-Condon factor for the 0–0 transition, and $\alpha_{\nu}^{\nu'}$ represents the Franck-Condon factor between initial $\nu$ and final $\nu'$ vibrational quantum numbers for vibrational mode $\alpha$. Diagonal vibronic coupling constants of (c) $S_0$@$S_1$ with vibrational mode 118 and (d) $S_0$@$S_2$ with vibrational mode 117 calculated within the crude adiabatic approximation [10].

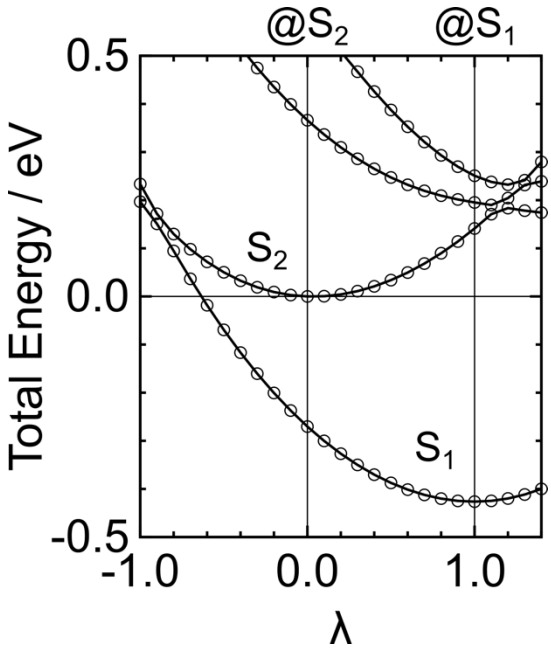


**Figure S25. Investigation of $S_1$ and $S_2$ state of MHTX.** Potential energy curves connecting the optimized $S_2$ and $S_1$ geometries: $E(R_\lambda)$ with $R_\lambda = (1-\lambda)R_{@S_2} + \lambda R_{@S_1}$, where $\boldsymbol{R}_{@S_2}$ and $\boldsymbol{R}_{@S_1}$ represent the Cartesian coordinates at the $S_2$ and $S_1$ geometries, respectively. The energy reference is the total energy of $S_2$@$S_2$ (-1078.9610 a.u.).

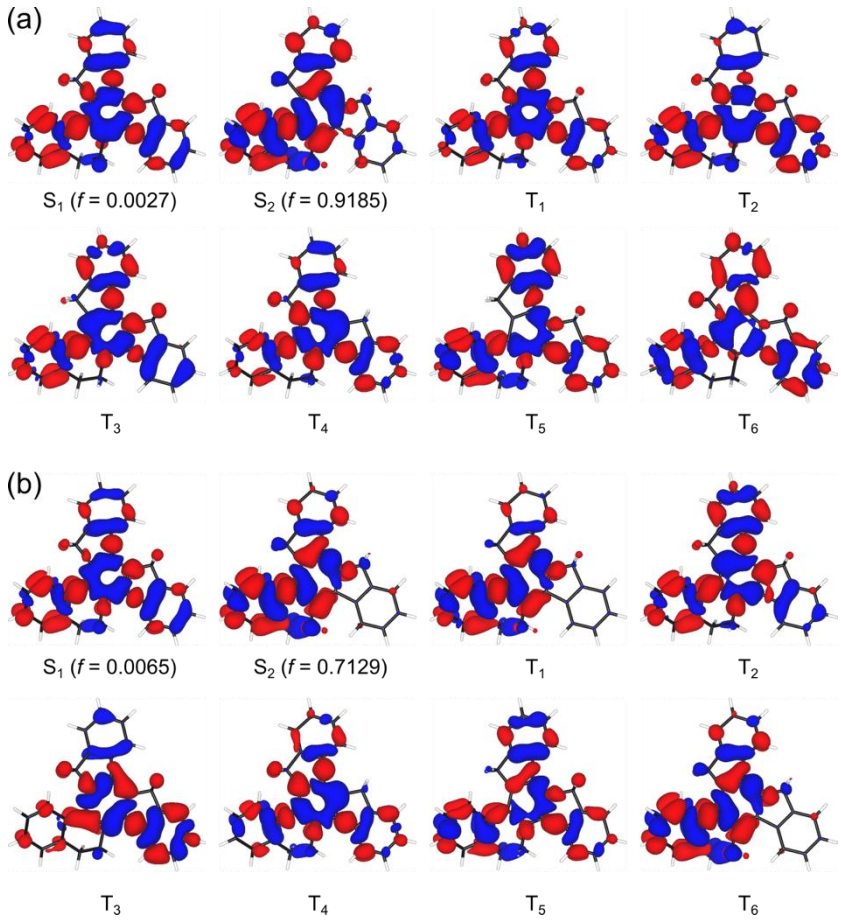


**Figure S26. Electronic density of radiative decays of MHTX.** Electron density differences for $S_m$-$S_0$ and $T_m$-$T_0$ at the (a) $S_1$ and (b) $S_2$ optimized structures (isosurface value: $5.0 \times 10^{-4}$ a.u.). Red and blue regions indicate positive and negative values, respectively.

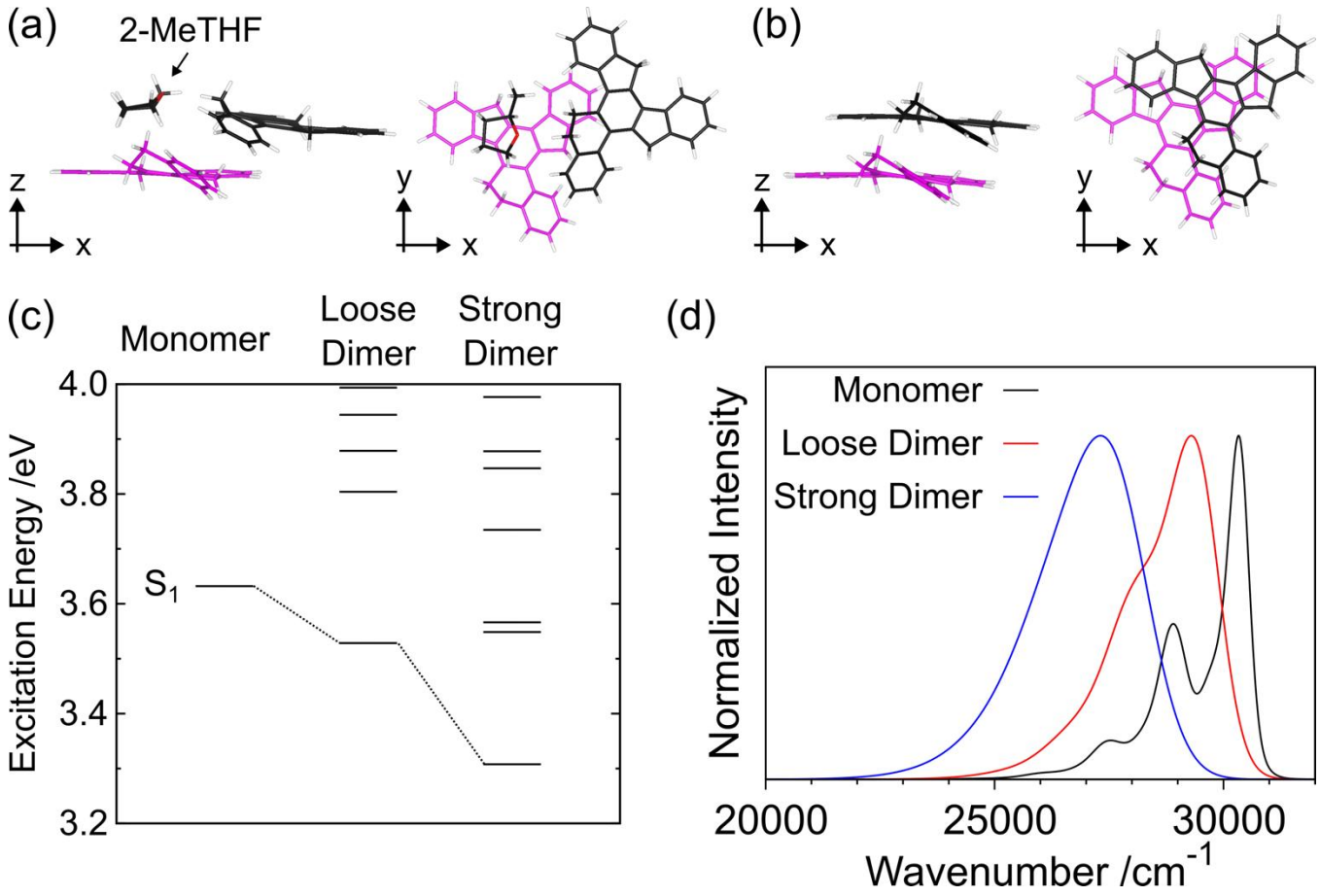


**Figure S27. Investigation of dimer formation.** $S_1$ optimized geometries of the (a) loose and (b) strong dimers. (c) Calculated energy levels of excited states at the $S_1$ optimized structure and (d) $S_1$ fluorescence spectra for the monomer, loose dimer, and strong dimer. The density of final vibronic states is expressed using a Gaussian function with a linewidth of 100 $cm^{-1}$ for the spectral calculations.

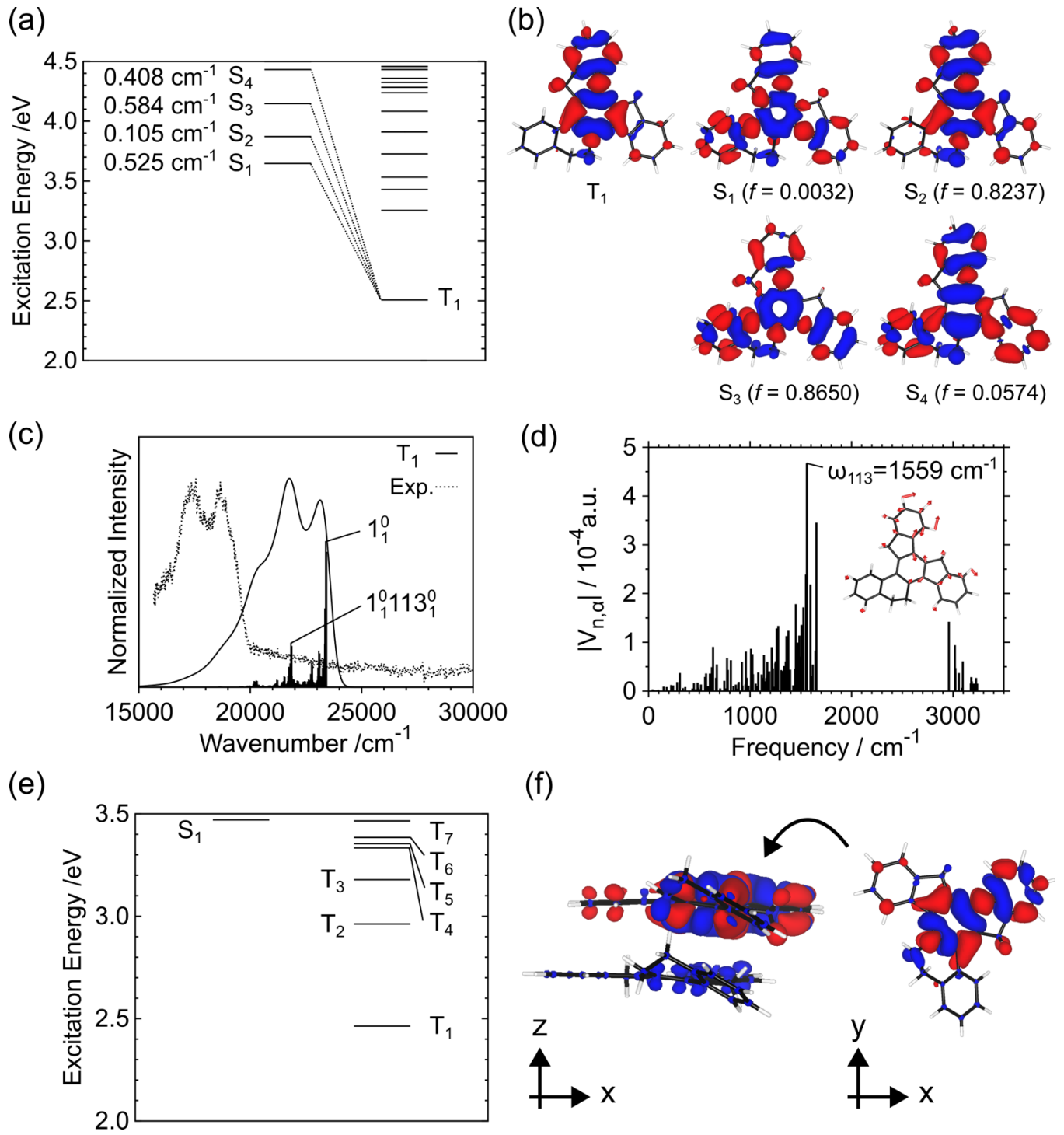


**Figure S28. Theoretical study of the triplet states of MHTX.** (a) Energy levels of excited states at the $T_1$ optimized structure for the monomer. Values represent the SOC matrix element between singlets and triplets. (b) Electron density differences for $S_m$-$S_0$ and $T_m$-$T_0$ at the $T_1$ optimized structure for the monomer (isosurface value: $5.0 \times 10^{-4}$ a.u.). Red and blue regions indicate positive and negative values, respectively. *f* represents the oscillator strength of $S_m$-$S_0$. (c) Calculated monomer phosphorescence spectrum from $T_1$ at $T$ =80 K (solid line), compared with the experimental spectrum (dotted line, Figure S17b). The density of final vibronic states is expressed using the Gaussian function with a linewidth of 300 $cm^{-1}$. Vertical lines represent the Franck-Condon factor, where $\alpha_{\nu,}^{\nu}$ represents the Franck-Condon factor between initial $\nu$ and final $\nu'$ vibrational quantum numbers for vibrational mode $\alpha$. (d) Diagonal vibronic coupling constants of $S_0$@$T_1$ with vibrational mode 113 calculated within the Born-Oppenheimer approximation[11]. (e) Excited states at the $T_1$ optimized structure for the strong dimer. (f) Electron density difference of $T_1$-$S_0$ at the $T_1$ optimized structure for the strong dimer. (isosurface value: $5.0 \times 10^{-4}$ a.u.)

## 6. References


1. Pyrko, A. Self-condensation of 6-Methoxytetralone. *ChemInform* **23**, (1992).
2. Williams, P. cis- and trans-Isomerism in 2-(1-indanylidene)indan-1-one. *ChemComm* 719–720 (1967)
3. Sharma, L. K., Kim, K. B. & Elliott, G. I. A selective solvent-free self-condensation of carbonyl compounds utilizing microwave irradiation. *Green Chemistry* **13**, 1546–1549 (2011).
4. Mueller, A. & Amsharov, K. Y. Synthesis of Robust Precursors for the Controlled Fabrication of (6,6), (8,8), (10,10), and (12,12) Armchair Single-Walled Carbon Nanotubes. *European J. Org. Chem.* **2015**, 3053–3056 (2015).
5. Amick, A. W. & Scott, L. T. Trisannulated Benzene Derivatives by Acid Catalyzed Aldol Cyclotrimerizations of Cyclic Ketones. Methodology Development and Mechanistic Insight. *J. Org. Chem.* **72**, 3412–3418 (2007).
6. Salla, C. A. M. *et al.* Persistent Solid-State Phosphorescence and Delayed Fluorescence at Room Temperature by a Twisted Hydrocarbon. *Angew. Chem. Int. Ed.* **58**, 6982–6986 (2019).
7. Jiang, H. *et al.* Effect of photo-oxidation on the emissive properties of truxene. *J. Photochem. Photobiol. A Chem.* **369**, 195–201 (2019).
8. Chen, F. *et al.* Density, viscosity, speed of sound, excess property and bulk modulus of binary mixtures of γ-butyrolactone with acetonitrile, dimethyl carbonate, and tetrahydrofuran at temperatures (293.15 to 333.15) K. *J. Mol. Liq.* **209**, 683–692 (2015).
9. Sengers, J. V. & Watson, J. T. R. Improved International Formulations for the Viscosity and Thermal Conductivity of Water Substance. *J. Phys. Chem. Ref. Data* **15**, 1291–1314 (1986).
10. Ota, W., Uejima, M. & Sato, T. Role of Vibronic Couplings and Energy Gap in the Internal Conversion Process of a Molecule. *Bull. Chem. Soc. Jpn.* **96**, 582–590 (2023).
11. Santoro, F., Improta, R., Lami, A., Bloino, J. & Barone, V. Effective method to compute Franck-Condon integrals for optical spectra of large molecules in solution. *J. Chem. Phys.* **126**, (2007).